

An Instrument For Investigation of the Cosmic Microwave Background Radiation at Intermediate Angular Scales

E. J. Wollack¹, M. J. Devlin, N. Jarosik,
C. B. Netterfield, L. Page, and D. Wilkinson

Princeton University, Department of Physics, Jadwin Hall, Princeton, NJ 08544

ABSTRACT

We describe an off-axis microwave telescope for observations of the anisotropy in the cosmic microwave background (CMB) radiation on angular scales between 0.5° and 3° . The receiver utilizes cryogenic high-electron-mobility transistor (HEMT) amplifiers and detects the total power in multiple 3 GHz wide channels. Both frequency and polarization information are recorded allowing discrimination between CMB radiation and potential foreground sources and allowing checks for systematic effects. The instrumental radiometric offset is small (~ 1 mK). Data are taken by rapidly sampling while sweeping the beam many beamwidths across the sky. After detection, a spatio-temporal filter is formed in software which optimizes the sensitivity in a multipole band in the presence of atmospheric fluctuations. Observations were made from Saskatoon, Saskatchewan (SK), Canada during the winter of 1993 with six channels between 27.6 and 34.0 GHz, in 1994 with twelve channels between 27.6 and 44.1 GHz, and in 1995 with six channels between 38.2 and 44.1 GHz. The performance of the instrument and assessment of the atmospheric noise at this site are discussed.

Subject headings: cosmic microwave background — cosmology: atmospheric effects: instrumentation — radiometry — telescopes

¹Present address: National Radio Astronomy Observatory, 2015 Ivy Road, Charlottesville, VA 22903.

1. Introduction

In most cosmological models, the anisotropy in the cosmic microwave background (CMB) is a direct probe of the conditions in the early universe. A complete characterization of the $\sim 30 \mu\text{K}$ signal can potentially tell us about the large scale geometry of the universe, the Hubble constant, the source of primordial density fluctuations, the fraction of the universe made of baryons, and the ionization history (Bond et al. 1994, Jungman et al. 1995). Measurements of the CMB anisotropy over a wide range of frequencies and angular scales are currently being conducted. Reviews of the results and theoretical issues may be found in Bond 1995, Readhead & Lawrence 1992, and White, Scott, & Silk 1994. In this paper, we describe a ground-based telescope that operates between 28 and 45 GHz and probes angular scales between 0.5 and 3 degrees (roughly between multipoles $l = 60$ and 360). Data have been taken with both K_a -band (28-34 GHz) and Q-band (38-45 GHz) receivers. Observations were made in the winters of 1993, 1994, and 1995 at an observing site in Saskatoon, Saskatchewan (SK), Canada. We refer to the results from the three years as SK93, SK94, and SK95. Previous results and limited information about the instrument are given in Wollack et al. 1993 (SK93), Wollack 1994 (SK93), Wollack et al. 1994, Page et al. 1994, Netterfield 1995 (SK94), and Netterfield et al. 1995 (SK93 to SK94 comparison). An analysis of the data from all three years is in Netterfield et al. 1996.

Figure 1 shows the configuration of the SK experiment. A mechanically-cooled HEMT-based (high-electron-mobility transistor) receiver senses the sky in three frequency bands and two polarizations. The beam is formed by a cryogenic feed and an ambient temperature off-axis parabola. The beam is steered on the sky by a large computer-controlled chopping plate that oscillates around a vertical at ~ 4 Hz. As the plate moves, the receiver outputs are rapidly sampled. The elevation of the beam is fixed at 52° , the latitude of Saskatoon, SK. To point the telescope, the receiver, parabola, near ground-screen, electronics, and chopping plate are moved in azimuth as a unit. All of the beam-forming optics are inside a large fixed aluminum ground-screen.

For all measurements of the anisotropy of the CMB, the signal is between 10^{-6} and 10^{-8} of the ambient temperature. Because it takes anywhere from a few hours to hundreds of hours of integration to

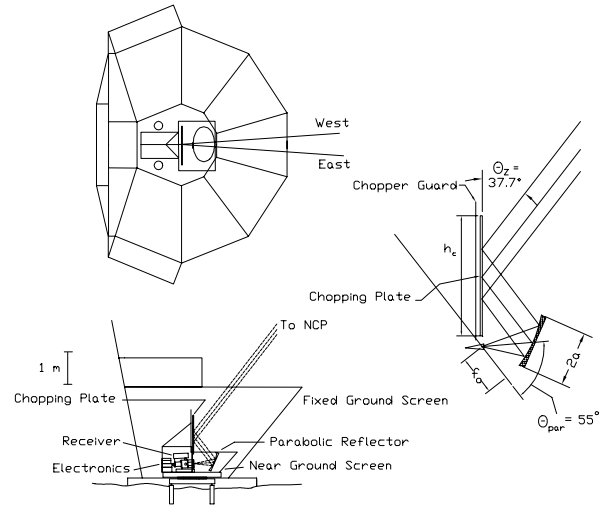


Fig. 1.— The observing setup in Saskatoon and the telescope geometry. On left top and bottom are plan and section views of the SK94 telescope and ground-screen. On the right is a detail of the beam forming optics.

distinguish the celestial signal from the atmospheric emission and instrument noise, great care must be taken to ensure that the signal is fixed to the sky and not due to a systematic effect buried in the instrument noise. Generally, systematic effects modulate the baseline or ‘offset’ of the radiometer. The offset is the instrumental contribution to a differential measurement of a uniform sky. In principle this is zero. In practice, it typically ranges between tens of micro-Kelvin to a few milli-Kelvin. It may be caused by atmospheric gradients, thermal or emissivity gradients in the optics, polarized emission from the optics, misalignment of the optics, asymmetric sidelobe contamination, microphonics, or electronic pickup. In most all experiments (one exception is the OVRO RING experiment Myers, Readhead, & Lawrence 1993), this term is subtracted from the data before analysis. The larger the offset, the more vulnerable the data are to the environment and quirks of the instrument. Just as important as the magnitude is the offset’s stability.

Since the discovery of the CMB, researchers have realized that the radiometric offset can be minimized by moving only the optical element furthest from the receiver (Partridge & Wilkinson 1967, Fabbri et al. 1980, Lubin, Epstein, & Smoot 1983, Davies et al. 1987, Dall’Oglio & de Bernardis 1988, Dragovan et al. 1994). If the beam is scanned only in azimuth, then

the atmospheric signal is minimized. The remaining dominant sources are modulated emission from and spill past the edges of the chopping plate. For the Saskatoon experiments, the offset depends on the year and the observing strategy. In 1993 and 1994, it was $\sim 400 \mu\text{K}$; in the worst case in 1995, it was 2.2 mK. The change in average offset was $< 7 \mu\text{K}/\text{day}$ for all observations.

For clarity, this paper focuses on the K_a -band system, but frequent references are made to the two different Q-band configurations that share the same observing platform. In Section 2 the receiver is discussed. In Section 3 we outline the telescope design and performance. Calibration, radiometric offsets, and atmospheric seeing are reviewed in Sections 4, 5, and 6 respectively.

2. The Receiver

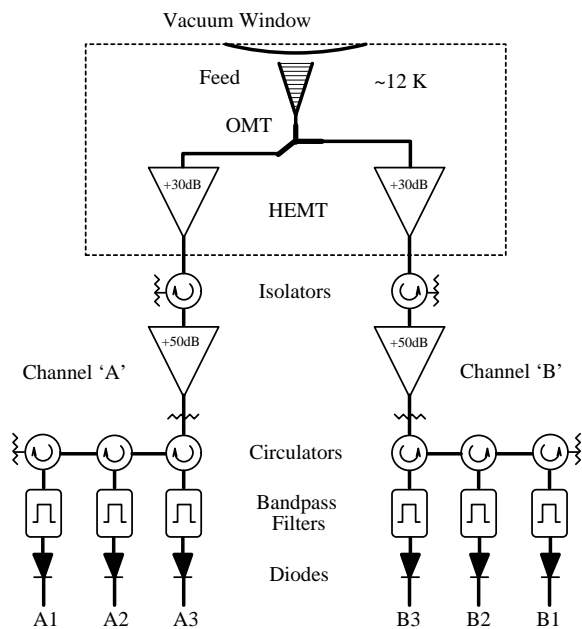


Fig. 2.— The SK93 K_a receiver layout. Radiation enters through the vacuum window and is collected by a cooled corrugated feed. It is then split into two orthogonal polarizations by the orthomode transducer (OMT). Each polarization is then amplified, separated into three frequency bands, and square-law detected.

The receiver is comprised of a mechanically-cooled dewar at 15 K, which houses the HEMT amplifiers and a single feed horn, and a thermally regulated 300 K enclosure, which houses the warm amplifiers and band-defining microwave components. Figure 2 shows a schematic of the K_a receiver. It operates in total-power, base band mode; that is, there are no Dicke switches, mixers, or local-oscillators. Similar receivers are discussed in Gaier et al. 1992 and Gundersen et al. 1994. The receiver is positioned so that the feed horn’s phase center is imaged to within 0.5 cm of the rotation axis of the chopper which is in turn near the center of a large fixed ground-screen. The geometry is shown in Figure 1.

2.1. Receiver RF Design

Radiation from the sky enters the receiver through a 9 cm diameter vacuum window made of 0.38 mm polypropylene. Two overlapping aluminum baffles define the entrance aperture. One is anchored to the ~ 70 K stage, the other to ambient temperature. Strips of aluminized Mylar electrically connect the top of the feed to the warm baffle and suppress RF interference. To inhibit the formation of frost on the vacuum window, warm air is forced into a volume in front of the window defined by a low loss polystyrene foam ring (Eccofoam PS, Emerson & Cuming Inc., Canton, MA) covered with a 0.09 mm polyethylene sheet.

The beam is formed by a conical corrugated scalar feed (See Clarricoats & Olver 1984 and references therein.). At the base of the feed, a wide band TE_{11} -to- HE_{11} mode converter (James & Thomas 1982, Wollack 1994) matches the hybrid mode to circular waveguide. Next, for the K_a system, an electroformed adiabatic round-to-square transition matches the feed to the orthomode transducer (OMT) which splits the incident radiation into vertical and horizontal linear polarizations. The low end of the feed’s bandpass is defined by the input waveguide cutoff and the upper end is set by the excitation of TM_{11}^o in the horn-to-circular-guide transition. Over the 26-to-36 GHz bandpass of the K_a receiver, the reflection coefficient is less than -26 dB and between 23 GHz and 48 GHz it is less than -20 dB. The Q-band feed for SK94 is scaled from the K_a -band design and has similar performance. The design parameters for all of the feeds are given in Table 1.

The outputs of the OMT are fed directly into two National Radio Astronomy Observatory (NRAO) am-

TABLE 1
SK TELESCOPE SPECIFICATIONS

	SK93K _a	SK94K _a /Q	SK95Q
Feed Semi-flare Angle, θ_o	6.0°	6.0°	4.4°
Feed Aperture Diameter, d_h	4.2 cm	4.2/3.0 cm	2.1 cm
Feed Normalized Phase Error, Δ	< 0.1	< 0.1	< 0.06
Feed Phase Center, $t(\nu_c)$	1.5 cm	1.5 cm/1.0 cm	0.24 cm
Feed Hybrid Frequency, ν_x	29.9 GHz	29.9/39.7 GHz	39.7 GHz
Feed Beamwidth, $\theta_{\text{feed}}^{\text{FWHM}}(\nu_x)$	18°	18°/20°	27°
Primary Edge Illumination	< -24 dB	< -24 dB	< -27 dB
Primary Offset Angle, θ_{par}	+55.0°	+55.0°	+55.0°
Primary Minor Axis, $2b$	58.4 cm	58.4 cm	122.0 cm
Primary Major Axis, $2a$	65.8 cm	65.8 cm	137.5 cm
Primary Focal Length, f_o	50.0 cm	50.0 cm	75.0 cm
Primary Surface Tolerance, Δ_{rms}	8 μm	8 μm	$\sim 10 - 20\mu\text{m}$
Primary Aperture Efficiency, $\eta_a(\nu_c)$	0.52	0.54	0.56
Primary Beamwidth on Sky, $\theta_{\text{beam}}^{\text{FWHM}}(\nu_c)$	1.44°	1.42°/1.04°	0.5°
Chopper Edge Illumination	< -45 dB	< -45 dB	< -30 dB
Chopper Shield Edge Illumination	< -65 dB	< -65 dB	< -50 dB
Far Ground-screen Edge Illumination	< -65 dB	< -65 dB	< -65 dB
Chopper Width, w_c	91.4 cm	91.4 cm	146.1 cm
Chopper Height, h_c	121.9 cm	121.9 cm	207.6 cm
Chopper Surface Tolerance, Δ_{rms}	< 40 μm	< 40 μm	< 40 μm
Chopper Aperture Efficiency, $\eta_a(\nu_c)$	0.16	0.17	0.27
Chopper Step Response Transition Time	29 ms	32 ms	—
Chopper Frequency, f_c (max)	10 Hz	6 Hz	3 Hz
Chopper Amplitude in AZ, ϕ_c (max)	$\pm 2.5^\circ$	$\pm 3.5^\circ$	$\pm 3.5^\circ$

plifiers (Pospieszalski et al. 1988, Pospieszalski 1992). These devices have approximately 10 GHz of available bandwidth and +30 dB of RF gain. When cooled to ~ 15 K, the average noise temperatures of the K_a and Q-band amplifiers are ≈ 50 K and ≈ 20 K respectively.

The HEMT amplifiers are connected to ambient temperature isolators by a 10 cm length of 0.25 mm wall stainless steel WR28 waveguide (WR22 for Q-band), gold plated to minimize attenuation. The waveguide vacuum windows between the refrigerator and the room temperature receiver box are made of 0.013 mm thick kapton sheet. Following the isolators are commercial wide-band amplifiers with $\sim +50$ dB of gain. These amplifiers have a noise figure of 4 – 7 dB. Split-block attenuators are used to flatten the bandpass and set the signal level presented to the diodes detectors in the K_a receiver. In the Q-band receiver, a relatively large HEMT gain slope and the frequency multiplexor design necessitated locating the level set attenuator before the room temperature amplifiers to avoid gain compression. In both receivers, the contribution to the total system temperature from the components after the HEMT amplifiers is < 2 K.

In the K_a receiver, half-wave waveguide filters and full-band circulators form a filter bank as shown in Figure 2. The ~ 10 GHz HEMT bandwidth is divided into three passbands in order to maximize spectral discrimination, passband flatness, and minimize noise. The highest usable frequency is set by the OMT. In the E-plane port (called A channels), spurious spikes due to the TM_{11}^{\square} mode in the OMT set the upper band edge at 35.6 GHz. The passband of the H-plane port (called B channels) smoothly degrades above 36 GHz. The highest frequency filters are tailored for maximum bandwidth in response to this difference. Some care must be taken with the lowest channel filter. Waveguide dispersion moves the ‘second harmonic’ of the filter response to lower frequencies than is expected in a TEM structure (Matthaei, Young, & Jones 1980). A ‘picket fence’ filter with a 26-to-32 GHz bandpass in series with the filter is necessary to prevent leakage near 38 GHz into the high frequency channels. The large number of waveguide joints in the filter bank make them especially prone to microphonics. This problem was overcome by embedding them in a mechanically stable and electrically lossy contoured support structure. In the Q-band system, all the filtering is done with a custom built, monolithic, channel-dropping multiplexor. A listing of the major components used in the two re-

ceivers is given in Table 2.

On the output of each waveguide filter is a negative polarity Schottky barrier diode. A typical sensitivity is 1500 mV/mW and the response is linear in power for input levels small compared to -10 dBm (with a 1 M Ω audio impedance). Optimal performance was achieved with -18 dBm of RF power at the diode. By tuning each chain’s split-block attenuator, all channels were within 3 dB of this value. The typical DC level out of a diode was ~ 20 mV. Mounted on the SMA output of each diode is a low-noise preamp with a gain of 100 and a 2k Ω input impedance. This impedance is a reasonable compromise between the reduction in sensitivity (compared to 1 M Ω) and increased signal linearity and thermal stability. The radiometer noise is approximately ten times the preamp noise floor.

2.2. Receiver Thermal and Mechanical Considerations

The cryogenic components are cooled by a CTI 350 refrigerator which allows uninterrupted operation of the receiver for extended periods of time. All mechanical and electrical connections from the cold stage to 300 K are thermally anchored to the refrigerator ~ 70 K stage. The bias wiring, waveguide connections to the room temperature receiver, and radiation loading of the refrigerator result in a total cold stage thermal load of 950 mW. With a CTI 8500 compressor, the cold stage runs at ~ 12 K, roughly 2 K warmer than without any thermal load. A rms thermal variation of ~ 40 mK synchronous with the refrigerator 1.2 Hz drive is measured at the cold station. This signature is not detected in the radiometer outputs.

By design, the cold stage vibrational amplitude is < 0.013 mm (CTI 1971). The vibration power spectrum is dominated by a 1.2 Hz line from the cold head cycle and by the broadband feature at ~ 200 Hz resulting from gas flow through the refrigerator. Slight changes in RF impedance caused by vibrations can be synchronously modulated by the chopper. This microphonic sensitivity was eliminated through the use of monolithic sub-assemblies, adequate strain relief throughout the receiver chain, and a waveguide flange alignment of < 0.05 mm. In particular, microphonics were traced to loose attenuator vanes, isolator tuning networks, and waveguide joints.

The room temperature receiver box is rigidly mounted on the dewar. It has two levels of RF shielding and is

TABLE 2
RADIOMETER COMPONENTS

	Component	Part Number	Source
SK-K _a	Orthomode Transducer	P/N OM3800	Atlantic Microwave Corp., Bolton, MA
	Cryogenic Amplifiers	S/N 6, 14	NRAO, Charlottesville, VA
	Circulators	P/N WFR-C	Microwave Resources Inc., Chino, CA
	Warm Amplifiers	P/N SMW92-1953	Avantek Inc., Santa Clara, CA
	Bandpass Filters ‘A’	P/N BFF-28-27.5, 30.5, 33.5	Dorado Int. Corp., Seattle, WA
	Bandpass Filters ‘B’	P/N F27.5-6, 30.5-6, 34.0-6	Spacek Labs, Santa Barbara, CA
	Diodes	P/N DXP-28	Millitech Corp., South Deerfield, MA
SK-Q	Orthomode Transducer	P/N 110265-1	Gamma $-f$ Corp., Torrance, CA
	Cryogenic Amplifiers	S/N B-32, B-33	NRAO, Charlottesville, VA
	Isolators	P/N 45162H-1000	Hughes, Microwave Prod. Div., Torrance, CA
	Warm Amplifiers	P/N DB93-0474	DBS Microwave, El Dorado Hills, CA
	Triplexers	P/N 3647	Pacific Millimeter Products, Golden, CO
	Diodes	P/N DXP-22	Millitech Corp., South Deerfield, MA

filled with microwave absorber to limit air convection as well as damp microwave energy. A G-10 fiberglass spacer mechanically supports the inner box and provides the thermal path between the boxes with a several hour time constant.

The diode sensitivity and amplifier gain are a function of temperature. Double regulation of the temperature of the receiver enclosure is required to allow field operation between -45°C and 0°C . The outside of the enclosure is regulated to $10\pm 2^{\circ}\text{C}$, while the inside is regulated at 28C to better than $\pm 0.035^{\circ}\text{C}$. In addition, the RF components are fitted with insulation to prevent convective cooling and are thermally anchored to a common aluminum mounting plate. With the inner regulator on, the gain coefficient is less than -0.03 dB/K for temperature changes on the outside of the receiver box.

2.3. Radiometer Noise and Passbands

We use two different means to measure the system noise in the laboratory. In the first method, a variation on the Y-factor technique (e.g. Pozar 1990), the power from a cold load is varied and the radiometer response is recorded for a series of points. Over the region of linear response, the sensitivity and noise are related to the slope and the intercept of the resulting data. This technique measures the mean noise power. In the second method, the audio frequency power spectrum of the calibrated receiver is measured directly with a spectrum analyzer. Only at frequencies

large compared to the receiver $1/f$ knee do these two methods give the same spectral noise density. The Y-factor test always yields a better sensitivity because it is insensitive to low frequency fluctuations.

In the power spectrum of the noise at the diodes, as shown in Figure 3, the $1/f$ character is readily apparent. This was shown to be due to gain fluctuations in the HEMT amplifiers (Jarosik et al. 1993). The total power spectral density is well modeled by a modified radiometer equation (e.g. Rohlfis 1990),

$$\frac{\Delta T}{T_{\text{sys}}} = \sqrt{\frac{1}{\Delta\nu_{\text{rf}}\tau} + \left(\frac{\Delta G(f)}{G}\right)^2}, \quad (1)$$

where $(\Delta G/G)^2 \propto 1/f^{\alpha}$ is the square of the fractional receiver gain variation. The dominant contribution to the gain fluctuations in the system is the cryogenic HEMT amplifier. The measured variations in the K_a band HEMT gain are, $(\Delta G/G) \sim 2 \times 10^{-5}$ at 8 Hz with $\alpha \simeq 0.9$. Both the magnitude of the fluctuations and α are weakly dependent on the transistor bias (Wollack 1995). A summary of the measured sensitivities is given in Table 3.

The gain fluctuations correlate data from different channels of a single amplifier chain. With the independent A and B polarizations, which are not correlated by gain fluctuations, one can distinguish between correlations due to a common source, for instance a fluctuating atmosphere, and those intrinsic to each amplifier. As the magnitude of the atmospheric fluctuations approaches the receiver noise

TABLE 3
RADIOMETER CENTROIDS, PASSBANDS, AND SENSITIVITY

	i [Channel]	ν_c [GHz]	$\Delta\nu_{\text{rf}}$ [GHz]	T_N^{a} [K]	$S_{\text{lab}}^{\text{b}}$ [mK sec $^{\frac{1}{2}}$]	$S_{\text{sky}}^{\text{c}}$ [mK sec $^{\frac{1}{2}}$]
SK93/94K _a	K _a -A1	27.6 ± 0.15	2.8 ± 0.2	44	1.1	1.6
	K _a -A2	30.5 ± 0.15	2.9 ± 0.2	38	1.5	1.9
	K _a -A3	33.4 ± 0.15	2.8 ± 0.2	53	1.3	1.6
	K _a -B1	27.5 ± 0.15	2.8 ± 0.2	29	1.1	1.5
	K _a -B2	30.5 ± 0.15	2.8 ± 0.2	47	1.3	1.7
	K _a -B3	34.0 ± 0.15	3.7 ± 0.2	51	1.4	1.7
SK94Q	Q-B1	38.2 ± 0.12	2.5 ± 0.1	< 10	1.8	2.3
	Q-B2	40.7 ± 0.12	4.1 ± 0.1	10		2.5
	Q-B3	44.1 ± 0.12	3.3 ± 0.1	15		4.0
SK95Q	Q-A1	38.3 ± 0.12	2.6 ± 0.1	21	2.5	3.5
	Q-A2	40.8 ± 0.12	2.3 ± 0.1	18	1.9	3.0
	Q-A3	44.8 ± 0.12	1.8 ± 0.1	24	2.9	5.1
	Q-B1	38.3 ± 0.12	1.8 ± 0.1	25	2.1	2.8
	Q-B2	41.1 ± 0.12	3.3 ± 0.1	22	1.3	1.7
	Q-B3	44.7 ± 0.12	2.5 ± 0.1	16	2.2	3.3

NOTE.—(a) The reported receiver noise temperatures, T_N , are measured at the OMT circular waveguide input flange. The uncertainty is ± 3 K. (b) Receiver noise (total power) measured in the lab at 8 Hz using a 15 K cold load for K_a and 20 K for the Q-band system. The increase over the ideal is due to imperfect passbands and ‘ $1/f$ ’ noise in the HEMT amplifier. The error is ± 0.2 mK sec $^{\frac{1}{2}}$. (c) System noise at 8 Hz while observing the sky. These results are for atmospheric noise cut levels of $\zeta = 4.5, 1.7,$ and 1.5 mK sec $^{\frac{1}{2}}$ deg $^{-1}$ for SK93/94K_a, SK94Q, and SK95Q. The sensitivity to CMB fluctuations is reduced by a factor of κ_3 due to the observing pattern lock-in (See Table 8).

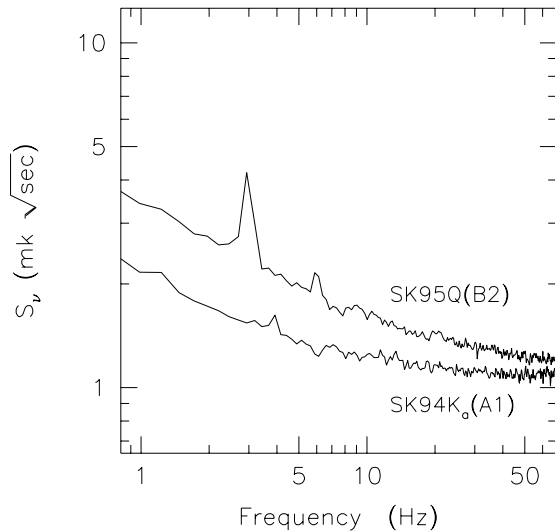


Fig. 3.— The power spectra, S_ν , of the receiver output. The data were taken while observing the sky during good weather. For SK95Q, the 2pt and 3pt offsets (See Sections 4.1 and 5) are manifest as the spectral features at 3 and 6 Hz ($\zeta = 1.5 \text{ mK sec}^{\frac{1}{2}} \text{ deg}^{-1}$). For SK94K_a, only the 2pt offset at 4 Hz is evident ($\zeta = 0.9 \text{ mK sec}^{\frac{1}{2}} \text{ deg}^{-1}$). Data taken under laboratory conditions have an indistinguishable $1/f$ component which originates from the cooled HEMT's. Given the approximately equal bandwidths in the K_a and Q systems, the higher Q-band $1/f$ knee reflects a lower gain stability. At $f \gg 100$ Hz the power spectra for both radiometers agree with the sensitivity derived from the measured RF bandwidth and system temperature.

floor, the cross-polarization frequency-frequency correlations ($\langle AB \rangle$) tend to zero, whereas the frequency-frequency correlations ($\langle AA \rangle$, $\langle BB \rangle$) approach the same value as measured in the lab with a cold load. Any inter-channel correlation, instrumental or atmospheric in origin, must be accounted for in assessing the statistical significance of the data (Wollack et al. 1993, Dodelson, Kosowsky, & Myers 1994).

The bandpass is determined by measuring the power response in each band with a leveled Hewlett Packard 8690B RF swept source at the orthomode transducer flange. It is defined as

$$\Delta\nu_{\text{rf}} = \frac{(\int_0^\infty G(\nu)d\nu)^2}{\int_0^\infty G(\nu)^2 d\nu}, \quad (2)$$

where G is the power response profile of the microwave band pass (Dicke 1946). In a typical channel, the bandpass ripple results in a $\sim 5\%$ reduction in sensitivity relative to an ideal filter response. Similarly, the center frequency is computed from

$$\nu_c = \frac{\int_0^\infty \nu T_b(\nu)G(\nu)d\nu}{\int_0^\infty T_b(\nu)G(\nu)d\nu}, \quad (3)$$

where T_b is the brightness temperature of the calibration source. The center frequency for a blackbody and a synchrotron calibration source (e.g. Cas A) differ by ~ 200 MHz for a typical channel. The effective bandwidths and center frequencies are given in Table 3.

2.4. The Data Collection System

A 80386-based computer located outside the fixed ground screen controls the telescope and data acquisition. The six receiver channels are read with V/F (voltage-to-frequency) converters on the telescope. Counter cards on the PC backplane synchronously ‘integrate’ the V/F output for each sample (See Table 4). To have sufficient dynamic range, each signal's DC level is removed by a low-noise bucking circuit and then amplified by a factor of five. The signals are filtered by eight-pole low-pass Bessel filters with a time constant determined by the sample rate. The system has an adjustable ~ 10 K data window. In practice, we find a 4 K window is sufficient for all the usable sky data (See Section 6). The chopper and base position are recorded at the same rate as the primary data. Housekeeping data are read by a 12 bit A/D in the PC at a slower rate. One master clock controls the V/F converters, the counter gates, and

TABLE 4
SK OBSERVING PARAMETERS

	SK93K _a	SK94K _a /Q	SK95Q
Elevation Angle, θ_{EL}	$+52.25 \pm 0.06^\circ$	$+52.16 \pm 0.06^\circ$	$+52.24 \pm 0.01^\circ$
Primary Beamwidth, $\theta_{\text{beam}}^{\text{FWHM}}(\nu_c)$	$1.44 \pm 0.02^\circ$	$1.42 \pm 0.02^\circ/1.04 \pm 0.02^\circ$	0.5°
Point Source Sensitivity, $\Gamma(\nu_c)$	$49 \mu\text{K Jy}^{-1}$	$50 \mu\text{K Jy}^{-1}/52 \mu\text{K Jy}^{-1}$	$230 \mu\text{K Jy}^{-1}$
Chopper Frequency, f_c	3.906 Hz	3.906 Hz	2.970 Hz
Sample Frequency, f_s	62.5 Hz	250 Hz	500 Hz
Sky Detection Frequency	12 Hz	8 – 32 Hz	6 – 70 Hz
Samples per Chop, N_s	16	64	168
Chopper Phase Offset, δN_s	$+0.6 \pm 0.1$	0.0 ± 0.1	0.0 ± 0.002
Bessel Filter Roll-Off, $f_{3\text{dB}}$	30 Hz	120 Hz	250 Hz
Beams per Throw	4	5/7	17
Chopper Amplitude on Sky, θ_t	$\pm 2.45^\circ$	$\pm 3.51^\circ/\pm 3.68^\circ$	$\pm 3.97^\circ$
Base Wobble Amplitude on Sky, θ_w	$\pm 4.91^\circ$	$\pm 4.42^\circ$	$\pm 4.50^\circ$
Observing Polarization, A B	$\updownarrow\leftrightarrow$	$\updownarrow\leftrightarrow/\dots\leftrightarrow$	$\updownarrow\leftrightarrow$

the chopper/base pointing update. In 1995, roughly 1 GByte/day of data were recorded. The telescope-control/data-acquisition PC is connected via Ethernet to a workstation where the data are stored, reduced and analyzed.

2.5. Electrical Offsets and Interference

Synchronous electrical pick-up and crosstalk in the system are small. A monitor diode and preamp in the receiver with a factor of 1×10^3 higher audio gain than the other channels indicates that synchronous electrical signals are less than $0.1 \mu\text{K}$. The receiver was tested in the lab with a regulated cold load as the radiation source while the chopper underwent a three position 4 Hz chop (more gentle motions were used in the field). This maximizes the chopper drive current and vibration. After a ~ 1 day coherent average of the data, an absolute upper limit of $< 10 \mu\text{K}$ is set on all audio frequencies of interest on any potential electrical or microphonic pick-up. In the field, the signal from the quadrature phase ² of the weighted data are stable and are typically $\sim 20 \pm 10 \mu\text{K}$; in worst case for SK95Q, $< 70 \mu\text{K}$.

The Saskatoon airport radar operates in L-band

²The quadrature phase, which is not sensitive to a signal on the sky, is shifted 90° relative to the chopper phase which is sensitive to the celestial signal. See Section 4

(~ 1 GHz) and sweeps our site every 8 seconds. This signal was not detected in the data or in the monitor channel at the $20 \mu\text{K}$ level. In the laboratory the receiver and data collection system were illuminated with a $+12$ dBm L-band source, again no signal was seen at the $10 \mu\text{K}$ level. There are no indications of RF interference in any of the data ³.

3. Antenna Design and Performance

An offset-parabolic reflector fed by a corrugated feed has minimal blockage, approximately equal E/H-plane beamwidths, and relatively low sidelobe response (Rudge et al. 1982). These properties are ideal for CMB observations. The radiometer beam is formed by a cooled corrugated feed horn which under-illuminates an ambient temperature parabola which in turn illuminates the chopping flat. There are two levels of ground-screen shielding: the near ground-screen moves with the beam-forming optics, shielding

³In the last decade the population of satellites using K_a-band communication channels has increased dramatically. There are now approximately 70 satellites in the Space Network Listing (RCB 1993) with on board equipment operating between 20 to 40 GHz. The bulk of these emit in our lowest frequency channel from geosynchronous orbits. Given typical satellite beam coverage, orbital parameters, and our scan strategy, the likelihood of RF contamination from a communications satellite is small.

the telescope base and decking, and the stationary far ground-screen shields the earth and sun. The telescope is optimized for observations at the elevation of the North Celestial Pole (NCP) from the site. See Figure 1 and Table 1 for a summary of the telescope geometry and system parameters.

3.1. Primary Illumination and The Main Beam

When an under-illuminated parabolic section is fed with a diffraction-limited feed, the resulting beam size is approximately frequency independent. This occurs because the competing effects of the diffraction-limited feed and the under-filled primary cancel. In this limit, the effective diameter of the primary illumination is inversely proportional to frequency.

For a corrugated feed with a small aperture phase error ⁴, the full-width-half-maximum (FWHM) beam width is

$$\theta_f \cong \sin^{-1} \left(\kappa_h \frac{\lambda}{d_h} \right), \quad (5)$$

where d_h is the effective aperture diameter and $\kappa_h \simeq 78^\circ$ is the beam constant for HE₁₁ aperture illumination ($\Delta \simeq 0.1$). To the same order of accuracy, the main beamwidth is given by

$$\theta_b \simeq \kappa_p \frac{\lambda}{d_p}, \quad (6)$$

where $\kappa_p \simeq 60^\circ$ is the beam constant for the primary illumination profile. We define $d_p \equiv 2f_{\text{eff}} \tan(\theta_f)$ as the effective primary illumination diameter and $f_{\text{eff}} \equiv 2f_o/(1 + \cos(\theta_{\text{par}}))$ as the distance from the focal point to the center of the off-axis parabolic section. Solving for the main beamwidth in the limit $\theta \ll 1$, we find

$$\theta_b(\nu) \approx \theta_b(\nu_c) \left[1 - \epsilon + \epsilon \left(\frac{\nu_c}{\nu} \right)^2 + \dots \right], \quad (7)$$

⁴The aperture phase error is the difference in wavelengths between the path from the feed apex to the edge of the aperture and from the apex to the center of the aperture (See for example, Thomas 1978). It is defined as

$$\Delta \equiv \frac{l_h}{\lambda} (1 - \cos \theta_o) = \frac{d_h}{2\lambda} \tan \left(\frac{\theta_o}{2} \right), \quad (4)$$

where l_h is the horn slant length, d_h is the aperture diameter, and θ_o is the horn semi-flare angle. Small Δ horns are diffraction-limited and thus have a frequency-dependent beam size. Large Δ feeds have a frequency-independent beam size (the phase error over the feed aperture effectively washes out coherence).

where

$$\theta_b(\nu_c) = \frac{\kappa_p}{\kappa_h} \frac{d_h}{2f_{\text{eff}}} (1 + \epsilon)$$

and

$$\epsilon = \frac{1}{2} \left(\frac{\kappa_h \lambda_c}{d_h} \right)^2 \ll 1.$$

The center frequency, ν_c , is ~ 30.5 GHz for K_a and ~ 41.0 GHz for Q-band. The approximate magnitudes of ϵ , are 0.051, 0.055 and 0.11 for SK93K_a, SK94Q and SK95Q respectively ⁵.

The telescope is focused by placing the feed phase center at the primary's focal point. For a corrugated horn the location of the phase center behind the plane of feed aperture, t , for the fundamental Gaussian mode can be expressed as (Martin 1990),

$$\frac{t}{l_h} = \frac{(\gamma\Delta)^2}{1 + (\gamma\Delta)^2}, \quad (8)$$

where $\gamma \equiv 2\pi\zeta^2 = 2.603$, l_h is the slant length of the horn, and Δ is the aperture phase error. Thus, for a small Δ horn, the phase center is near the aperture of the horn, while for large Δ horns the phase center is near the apex. The change in the position of the phase center with wavelength is given by

$$\frac{\partial t}{\partial \lambda} = -\frac{2l_h}{\lambda} \frac{(\gamma\Delta)^2}{1 + (\gamma\Delta)^2} \left(1 - \frac{(\gamma\Delta)^2}{1 + (\gamma\Delta)^2} \right). \quad (9)$$

Designs for frequency-insensitive waist positions exist for $\Delta > 1.8$ and $\Delta < 0.2$. We require that the change in waist position between 26 and 36 GHz is less than, $\sim 1\lambda$, the allowed defocusing error. During the alignment of the optics, the horn position that maximizes the forward gain in the center channel was used as the effective focal point. As a result, the upper and lower frequency channels are not optimally focused but the average instrument gain is maximized. The best horn position was insensitive to $< 1.5\lambda$ changes, consistent with the modeled prediction.

The telescope angular response was computed by aperture integration (Sletten 1988). We model the near field feed amplitude and phase with the first 20 modes in a Gauss-Laguerre expansion (Friberg,

⁵Equation 7 suggests that in order to reduce the main beam frequency dependence, the overall size of the optical system should be as large as possible for a fixed θ_b . The residual contributions to the beam's frequency dependence that arise from non-ideal feed performance and finite edge illumination should also be considered in this limit.

TABLE 5
SK MEASURED AND MODELED BEAMWIDTHS

	FWHM	A1/B1	A2/B2	A3/B3	σ_θ
SK93K _a	$\theta_x \simeq \theta_y$	1.46°	1.44°	1.41°	$\pm 0.02^\circ$
SK94K _a	$\theta_x \simeq \theta_y$	1.44°	1.42°	1.41°	$\pm 0.02^\circ$
Modeled	$\langle \theta_b(\nu_c) \rangle$	1.47°	1.44°	1.41°	$\pm 0.03^\circ$
SK94Q	θ_x	1.09°	1.08°	1.07°	$\pm 0.02^\circ$
	θ_y	1.012°	1.004°	0.993°	$\pm 0.006^\circ$
Modeled	$\langle \theta_b(\nu_c) \rangle$	1.06°	1.04°	1.00°	$\pm 0.03^\circ$
SK95Q	θ_x	0.471°/0.486°	0.443°/0.461°	0.453°/0.496°	$\pm 0.01^\circ$
	θ_y	0.567°/0.538°	0.525°/0.513°	0.570°/0.591°	$\pm 0.01^\circ$
Modeled	$\langle \theta_b(\nu_c) \rangle$	0.513°	0.505°	0.499°	$\pm 0.02^\circ$

NOTE.—The best fit to the measured beam-widths in the vertical and horizontal planes are denoted by θ_y and θ_x (The E-plane for the ‘A’ polarization is along θ_y and for ‘B’ it is along θ_x). The modeled full-width-half-maximum response, θ_b , is given for the center frequency for the design geometry. The uncertainty reflects the variation in beam-width with polarization and cut plane (E, H, and diagonal), and the uncertainty in the aperture illumination and telescope alignment. The discrepancy between the modeled and measured response for the SK95Q beam results from a 0.4 cm spacer (inadvertently omitted during alignment) which vertically shifted the feed in the focal plane from the design geometry. The observed increase in the beamwidth along θ_y and decrease along θ_x is consistent with the phase center offset.

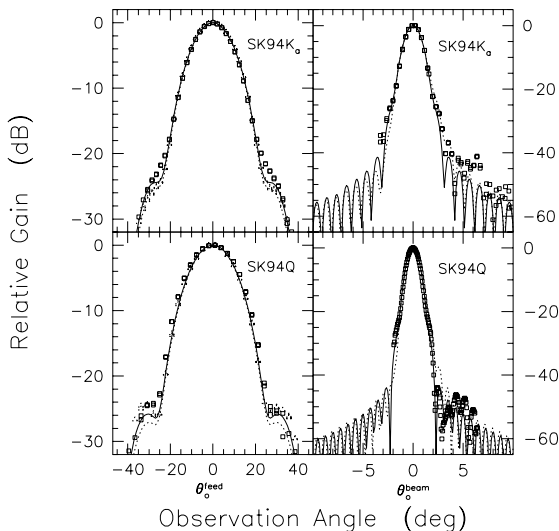


Fig. 4.— The SK94 main beam and feed horn response. The measured and theoretical response for the corrugated feed horns used in the K_a and Q -band systems are presented in the left panels. The solid lines are the E-plane and the dashed lines are the H-plane response. The right panels display the measured and computed telescope main beam maps. The theory curves were computed by aperture integration of the modeled feed illumination and phase. For clarity, only the measured main beam E-plane data for the horizontal polarization (channel B) is plotted. All measurements are at the feed hybrid frequency ν_x (See Table 1).

Jaakkola, & Tuovinen 1992; Tuovinen 1992) and integrate the resulting fields in the chopper plane ⁶. Figure 4 shows a comparison between the computed and measured beam profiles. A summary of the main beamwidth for each channel and polarization is given in Table 5.

The A and B polarizations were characterized in both the E and H-plane by illuminating the telescope with a coherent RF source. The far ground-screen, which has negligible effect on the main beam, was not present during this measurement. The measured beam efficiency, $\eta_b \simeq 0.99 \pm 0.01$, is in agreement with the model ⁷. After correction for the 80 m source-to-observation distance (Silver 1949), the measured and computed beamwidths agree to within $\sim \pm 2\%$. The magnitude of this correction is $\ll 1\%$, 0.4% , and 12% respectively for the SK93K_a, SK94Q, and SK95Q main beamwidths. The computed magnitudes are used to predict the optical performance. However, for the data analysis we rely on celestial calibrators to characterize the telescope angular acceptance.

The dominant source of cross-polarization in the telescope is the off-axis parabola. Its computed value is -24 dB (Rudge & Adatia 1978). The orthomode provides greater than -35 dB isolation between the A and B polarizations. The corrugated feed cross-polar pattern is intrinsically limited by the slot geometry and throat design to -40 dB (Clarricoats & Olver 1984, Dragone 1977) over our observing band. These effects introduce a correlation coefficient of ~ 0.004 between the A and B channels which is small com-

⁶We ignore the effects of the feed choke rings and vacuum window in the calculation. For the parabola, the longitudinal aperture currents are ignored. This introduces a $\lambda/16$ path-length error for observation angles

$$\theta_o^{\text{beam}} > (f_{\text{eff}} \lambda / 2b^2)^{1/2} \simeq 10^\circ, \quad (10)$$

from boresight, where $2b$ is the primary's major axis. At angles large compared to this value, the sidelobes are determined by the details of the primary, chopper, and ground-screen edge illumination, phase, and fabrication tolerances.

⁷For the SK telescope the aperture diameter is defined by the parabola edge. The parabola's illumination function encompasses the first null of the feed pattern over the entire RF bandwidth. In this limit, the beam efficiency is equal to the feed beam efficiency. In estimating the total main beam solid angle we integrate out to $2.5\theta_{\text{FWHM}}$. This is approximately the position of the first null in the response in the limit of a vanishing aperture phase error. The modeled magnitude includes the estimated ohmic, diffractive, and depolarization losses intrinsic to the telescope. The atmospheric transmission efficiency at the site (which can be derived from Figure 12), is not included in η_b .

pared to the atmospheric correlations.

The primary used for SK93/94 is machined out of a solid QC7 aluminum plate. The final surface has a rms of $8\mu\text{m} < 0.001\lambda$ (Crone 1993). The SK95 mirror (Fixsen 1995) was made out of 6061-T6 aluminum plate in 9 pieces, a 58 cm center section surrounded by 8 petals with a $\sim 10 - 20\mu\text{m}$ rms surface.

3.2. The Chopping Flat

A large flat aluminum honeycomb plate driven by custom voice coils sweeps the beam across the sky in azimuth⁸. A computer sends the requested position signal to a PID (Proportional Integral Derivative) control loop similar to that used by Payne (1976) and Radford et al. (1990). A high power op-amp drives current through the coils in response to an error signal (e.g. Kuo 1991).

A schematic of the chopper is shown in Figure 5, and the components and dimensions are given in Tables 1 and 6. Coils are wound on and epoxied to a Kevlar substrate which is in turn epoxied to the back of the chopping flat. The rotation axis of the assembly is adjusted to be at the center of mass, thus the front surface moves a small amount laterally as the chopper rotates. The coils are positioned so that an impulse produces minimal force on the pivot. Permanent magnets are mounted to a reaction bar which is also pivoted at its center of mass. A second set of ‘coupling’ coils couples the reaction bar to the frame using a PD control loop. Without them, the reaction bar hits the chopper mount when the telescope base is rotated.

When the coupling coils are turned off, the reaction bar and chopping plate are well modeled as a driven linear oscillator (Radford, Boynton, & Melchiorri 1990). The driving force is $F = 2\pi\rho N_{\text{eff}}iB$ where ρ is the radius of the coil, N_{eff} (≈ 120 turns) is the number of turns in the magnetic field B (≈ 2000 G), and i is the peak current through the coils. For the SK94 chopper, the force is approximately 30 N. Air resistance is negligible. An good estimate of the chopper throw is $\phi_c(\text{max}) \approx 2rF/I\omega^2$ where I is the moment of inertia, r is the distance from the center of the plate to the coils, and ω is the drive frequency. Using the values in Table 6, $\phi_c(\text{max}) \approx 4.3^\circ$ whereas the actual value was 3.5° . The measured

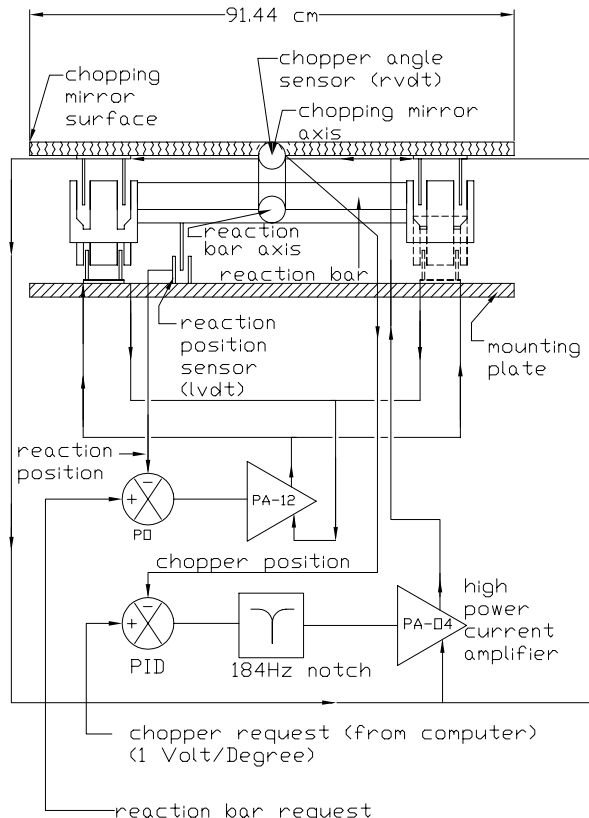


Fig. 5.— Top view of the SK94 chopper. The chopping flat and the reaction bar are separately mounted at their centers of mass with flex pivots. A notch filter removes frequency components from the error signal that are near the 184 Hz bending moment of the plate. The angle of the reaction bar is measured with a LVDT.

⁸The design is an extension of smaller choppers built at Princeton by M. Dragovan, J. Peterson, and G. Wright. We benefitted from their insights and previous work.

TABLE 6
SK94 CHOPPER COMPONENTS

Assembly	Subassembly Part Number	Physical Characteristics Source
Chopping Plate	Chopper Flat Al Honeycomb	Thickness = 2.59 cm (Front/Back Face=0.305 mm/0.406 mm) Mass = 5.8 Kg, I = 0.36 Kg-m ² Shape: 3' by 5', approximately ellipsoidal M.C. Gill Co., El Monte, CA
	Flex Pivots P/N 5016-800	Diameter = 1.27 cm Lucas Aerospace, Utica, NY
	Angle Encoder P/N RSYN-8/30	RVDT (rotary variable differential transformer) Lucas-Schaevitz, Pennsauken, NJ
	Servo Drive PA-04	Nominal 4Hz Triangle: ± 70 VDC @ 3.4 A (rms) Apex Microtechnology Corp., Tucson, AZ
Reaction Bar	Flex Pivots P/N 5024-400	Diameter = 1.91 cm Lucas Aerospace, Utica, NY
	Position Encoder Model 503XS-A	LVDT (linear variable differential transformer) Lucas-Schaevitz, Pennsauken, NJ
	Servo Drive PA-12	Nominal 4Hz Triangle: ± 15 VDC @ 1.4 A (rms) Apex Microtechnology Corp., Tucson, AZ
Coils/Magnets	Coil # 24 Ga. Cu Wire	Resistance = 13.5 Ω , Inductance = 20 mH Diameter = 7.9 cm, Axis Distance = 29 cm
	Permanent Magnets NdFeB, Grade 35	Diameter = 5.08 cm, Length = 4.76 cm Magnetic Sales and Mfg., Culver City, CA
	Yokes CMI-C Low Carbon Iron	Diameter = 12.7 cm, Length = 12.7 cm Connecticut Metals Incorp., Waterbury, CT

10% to 90% response time is ~ 30 ms. Though the chopper can be square-wave chopped; sinusoidal and rounded triangle motions are used for observing because they result in lower frame vibration and require less electrical power.

The azimuthal angle of the flat is measured with respect to the frame with a RVDT (rotary variable differential transformer) calibrated to 0.006° with the absolute encoder that measures the base motion. The angle is sampled at the data rate. For SK93/94 the chopper angle varied by less than 0.01° from the requested position. For SK95, the chopper size was increased from $91\text{ cm} \times 123\text{ cm}$ to $146\text{ cm} \times 208\text{ cm}$. Springs were attached to the flat and it was driven on resonance at 3 Hz. This led to a large reduction in the required power (SK94/SK93: 200 Watts, SK95: 25 Watts, despite the increase in size) but degraded positioning. At the worst times, the rms deviation from the requested position was 0.045° . This has no measurable effect on the data.

The magnetic fields of the chopper have been mapped and do not interfere with the receiver. The DC field within each magnet assembly is $\approx 2000\text{ G}$ over a 200 cm^3 volume and drops to less than 5 G at 20 cm . The permanent fields are oriented so that the AC components produced by the coils are in opposite directions near the receiver. At the receiver, the field at 3.9 Hz is 0.02 G .

The coils heat when the chopper is running and are cooled with DC fans. Seven sensors monitor the temperature distribution of the front of the plate. The temperature difference between the center to the coil position is about 7 K over 26 cm and is constant.

The surface of the chopping plate is not perfectly flat. At $\sim 2.5\text{ cm}$ scales, the deviations are random with a root-mean-squared amplitude of $< 40\ \mu\text{m}$. This results in a transfer of < 0.005 of the relative forward gain into diffuse sidelobes (See Ruze 1966; also, Dragone & Hogg 1963 for effects on the wide-angle antenna response.). Print-through of the aluminum honeycomb hexagon pattern produces a periodic array with a $\lambda_{\text{hex}} = 0.6\text{ cm}$ wavelength and amplitude of $4\ \mu\text{m}$. An absolute upper bound on relative gain loss of < 0.03 is computed by increasing the Ruze estimate the total number of scatters, $N \sim (D_{\text{mirror}}/\lambda_{\text{hex}})^2$. The measured beam maps do not have visible grating-lobes every $\lambda/d_{\text{eff}} \approx 2^\circ$, indicating the deviations are not particularly coherent across the aperture. These surface irregularities have an insignificant effect on the telescope forward gain and sidelobe response.

3.3. The Ground-Screens

The near and far ground-screens both block the relatively bright signals from the Earth and Sun and reflect the antenna sidelobes to cold sky. The far ground-screen size and angle are designed to shadow the top edge of the chopper baffle for incident rays greater than the angle at which undiffracted rays are reflected normal to the panels (see Figure 1). The far ground-screen is $> 17^\circ$ from the main beam, a clearance of > 3.5 times the parabola width. The ground-screen is fabricated out of aluminum angle and $1'' \times 4' \times 8'$ sheets of metalized housing insulation (Energy Shield, Atlas Roofing Company, Meridian, MS). The metal foil covered side of this housing insulation has an antenna temperature measured at 31.4 GHz of $\sim 320\text{ mK}$ for a 45° incidence angle. This is a factor of ~ 1.2 times the emissivity computed from the DC conductivity of the aluminum surface. Deviations in the surface of this material are on the order of 0.2 cm over a span of a few centimeters and large scale camber errors are not uncommon. In effect the sky, which has an order of magnitude lower antenna temperature than the ground, is being used as a termination for the sidelobes.

The sidelobe response of the telescope, including the near and far ground-screens, was measured. The structure was illuminated by a $\theta_{\text{FWHM}} = 7^\circ$ coherent RF source placed at eight locations around the perimeter of the ground-screen and on the roof a building behind the ground-screen. The source was pointed $\sim 9^\circ$ upward from horizontal, aimed at the edge of the closest panel, from 12 m away. It was modulated by a ‘hand chopped’ AN 73 Eccosorb (Emerson Cuming, Canton, MA) sheet in front of the transmitting horn. The measured sidelobe level is less than -115 dB for rays impinging upon the ground-screen from behind⁹. For rays illuminating the front ground screen edges, the response was $\sim -95\text{ dB}$. When the mirror is chopped, the demodulated signal was measured to decrease $\sim 10\text{ dB}$ in the E and H-planes relative to the direct signal from the source. Similar results were obtained for the Q-band system at 39.5 GHz . The attenuation provided by the ground-screen, found by measuring the response to a source directed at the telescope with and without the ground-screen erected, is greater than 36 dB . Leakage through the lower seams and panel glue joints limit

⁹The sidelobe level is measured relative to power received by the main beam, $10 \log(P_\theta/P_0)$.

TABLE 7
SK93K_a OFFSET AND SPILL ESTIMATES

	T_{phys} [K]	Constant [mK]	Modulation Source	Offset [μ K]
$T_{\text{electronic}}$	—	—	C/W	< 10
$T_{\text{microphonic}}$	—	—	C/W	< 10
$T_{\text{horn}}^{\text{e}}$	12	300	—	—
$T_{\text{window}}^{\text{e}}$	260	20	—	—
$T_{\text{parabola}}^{\text{e}}$	260	300	—	—
$T_{\text{plate}}^{\text{e}}$	260	400	C	< 300
T_{gs}^{e}	260	2	C/W	< 1
$T_{\text{atm}}^{\text{e}}$	260	15000	C/W	< 200
$T_{\text{parabola}}^{\text{s}}$	15	100	W	< 10
$T_{\text{plate}}^{\text{s}}$	15	20	C/W	< 10
T_{gs}^{s}	260	20	C/W	< 10

NOTE.—The physical temperatures of the emitting object, T_{phys} , are representative of the average magnitude. Temperatures with a superscript ‘e’ are due to emission. Temperatures in the table with a superscript ‘s’ are due to antenna spill. ‘Constant’ is the absolute radiometric brightness. Entries denoted with a ‘W’ and ‘C’ indicate modulation by the base wobble and the chopper motion respectively. The offsets are for the three-point data.

the net attenuation. The maximum ‘anisotropy’ emission from the ground screen is estimated to be less than $1\mu\text{K}$ (See Table 7).

With the exception of the sun, most foreground sources are more homogeneous than the test source. To the extent signals are not blocked by the ground-screens and are inhomogeneous after spatial averaging by the telescope sidelobes, a difference signal is produced. The K_a beam solid angle is $\sim 10^{-4}$ Sr. The sun is a 8200 K source at ~ 1 cm with a solid angle of 6×10^{-5} Sr (Allen 1976). Thus, a sidelobe level of ~ -100 dB is required to give a response of $\sim 1\mu\text{K}$ from incident solar radiation. For the Earth, a 300 K source subtending 2π Sr, a sidelobe of ~ -130 dB is required if a complete modulation of the incident radiation is assumed. Conservative analytical estimates indicate that differential contributions to the antenna temperature from the sidelobes are $< 10\mu\text{K}$. A host of effects enter at this level: signals can result from diffracted earth/sun-shine, changes in sidelobe illumination with base position, and gradients in the ground-screen panel temperature and emissivity.

In 1993, the ground-screen did not geometrically block the sun when it was directly behind the rear corners (See Figure 1). Once the problem was noticed, the ground-screen was modified. To be conservative, data taken with the sun illuminating the top of the chopper were blanked (Wollack et al. 1993). Independent of this precaution, for a given position on the sky, data recorded during the day and night are in agreement and the telescope offsets are independent of the time of day. To accommodate the size of the SK95 optics, the front edges of the far ground-screen were extended 46 cm and rolled with a radius of curvature of $r \simeq 23$ cm, to reduce the level of diffracted radiation (Keller 1959). With these modifications, the net shielding from the front section of the far ground-screen is similar to the level used in SK93/94.

4. Flux Scale Calibration and Pointing

The primary calibrator for both the K_a and Q radiometers is Cassiopeia A ¹⁰. Telescope efficiency and atmospheric attenuation are intrinsically included. The calibration signal is on the order of ~ 10 mK; thus, receiver non-linearity is not significant. To determine the beamwidth and pointing, the beam is swept in azimuth with the chopper while the earth’s

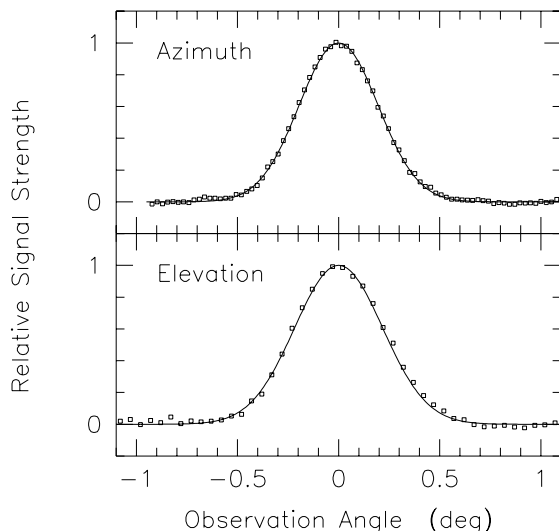


Fig. 6.— The SK95Q beam width determination from Cas A. Solid lines indicate the best fit Gaussian profiles of the beam. The open squares are the radiometer output.

rotation moves the source through the beam. The data are reduced with an optimal filter for a point source to make a two dimensional map of Cas A. See Figure 6. A two dimensional Gaussian is then fitted to determine the beamwidth and pointing. A summary of measured beamwidths is given in Table 5. The pointing is stable for the duration of an observing trip, attesting to the rigidity and stability of the telescope platform and footings.

The flux density scale for Cas A was obtained by fitting a power law to data compiled by Baars et al. 1977 from 8.2 GHz to 31.4 GHz and a measurement by Mezger et al. 1986 at 250 GHz. We find $S_\nu(\text{Cas A}) = (2070 \pm 162)\nu^{-0.695 \pm 0.029}$ Jy, where ν is the frequency in GHz (epoch 1994). A secular decrease of the form, $\eta = (0.9903 + 0.003 \log(\nu))^{N_t}$ (Baars et al. 1977), where N_t is number of years since the measurement, is assumed in correcting the Cas A flux scale to the observing epoch. The measured point source sensitivity of the telescope, $\Gamma = \lambda^2/2k\delta\Omega_a$, where $\delta\Omega_a$ is the total beam solid angle ¹¹, is used in assigning the flux scale. See Ta-

¹¹The beam solid angle, 4π divided by the directivity of the antenna, is related to the main lobe solid angle by $\delta\Omega_b = \eta_b\delta\Omega_a$, where η_b is the beam efficiency.

¹⁰3C461, 2321+583 IAU(1950), $l = 111.7^\circ$, $b = -2.1^\circ$

ble 4 for the magnitude of $\Gamma(\nu_c)$ at the synchrotron-spectrum weighted centroid, ν_c . Once the flux scale is assigned, the data are converted to the CMB thermodynamic temperature scale by dividing by the derivative of the Planck function with respect to temperature $(\partial T_{\text{ant}}/\partial T_{\text{CMB}})_{\nu} = x^2 e^x / (e^x - 1)^2$, where $x \equiv h\nu/kT_{\text{CMB}}$. Using $T_{\text{CMB}} \cong 2.726$ K (Mather et al. 1994, Gush et al. 1990), the conversion factors to the CMB temperature scale are 1.02 and 1.05 for 27.5 GHz and 44.1 GHz respectively.

The error in the temperature scale is dominated by the uncertainty in the knowledge of the flux of Cas A and its environment. Cas A passes through an elevation of 52.24° twice a day. For Q-band there was $\sim 7\%$ discrepancy and for K_a a $\sim 12\%$ discrepancy between the results of measurements taken in the morning and those taken in the evening. This effect is due to 2311+611, a ~ 25 Jy HII region (Kallas & Reich 1980, Fich 1986, Becker, White, & Edwards 1991), which is intercepted by the beam during the evening runs, but not during the morning runs. The uncertainty in our measurement of the relative temperature scale of Cas A is $\sim 5\%$, effecting all channels about equally, and the uncertainty in the spectral index is ± 0.1 . The temperature scale derived from measurements of Cas A are within 20% of the laboratory sensitivity measurements. The calibration is also affected by small errors introduced by inaccuracies in the beam θ_{FWHM} (2%), the phase of the recorded signals with respect to the optical axis ($< 1\%$), and the finite size of Cas A ($\ll 1\%$). The combination of all of these errors leads to a $\pm 14\%$ uncertainty (1 σ) in the CMB temperature scale. Reduction of this error will require a more accurate determination of the flux of Cas A.

4.1. Observing Strategy and Beam Synthesis

To measure the sky, the beam is swept in azimuth with a computer commanded pattern, \mathbf{x}_a , with frequency f_c and amplitude θ_t on the sky.¹² As a second level of modulation, the base is pointed at \mathbf{x}_o , θ_w west of the North Celestial Pole (NCP) for ~ 20 seconds and θ_w east of the NCP for ~ 20 seconds in a manner similar to Timbie & Wilkinson 1990. The instantaneous beam position is given by

$$\hat{\mathbf{x}}'(t) = \mathbf{x}_o(\theta_w, t) + \mathbf{x}_a(\theta_t, t), \quad (11)$$

¹² The chopper azimuth, ϕ_c , is related to sky throw by, $\theta_t \simeq 2\phi_c \cos(\theta_{\text{EL}})$, where θ_{EL} is the beam elevation.

where \mathbf{x}_o and \mathbf{x}_a are parallel to the horizon. Data taken with \mathbf{x}_o in the east and west base positions are analyzed independently.

The repositioning of the telescope base in azimuth, or wobbling, allows observation of the same patch of sky approximately every 12 hours. Thus a real sky signal can be differentiated from a residual 24 hour diurnal effect in the data set. This symmetry on the sky is not quite perfect because circles of constant elevation are not great circles. Nevertheless, the symmetry is good enough to provide convincing systematic checks. Due to the geometry of the ground-screens, a signal produced by the sun is expected to follow a 9 Hr-15 Hr-9 Hr cycle. If such a signal were present, it would be stronger in either the east or west and would interchange in base position from morning to evening. No such signals were observed.

In order to probe a range of angular scales the beam is scanned many beamwidths while rapidly sampling. By specifying the relative weight of each sample in software, an effective antenna pattern can be synthesized. For instance, if the samples with the chopper positioned in the west are weighted with ‘ -1 ’ and the east samples are ‘ $+1$ ’, the beam pattern resembles a classic single difference. Consider a weighting vector of the form

$$w_i(n) = \sum_{m=1}^{m(\text{max})} a_m \cos(m\omega_c t_i + \delta\phi_s) + b_m \sin(m\omega_c t_i + \delta\phi_s), \quad (12)$$

where $\omega_c \equiv 2\pi f_c$. The time samples

$$t_i = (i(\hat{\mathbf{x}}') - 1/2) / f_c N_s, \quad (13)$$

are evaluated at the midpoint of each integration bin, where i is the time sample index and N_s is the total number of samples in a chop. A phase difference between the chopper motion and the recorded data stream, $\delta\phi_s = 2\pi \delta N_s / N_s$, results from the mechanical and electrical responses.

With our chopper phase convention, the a_m (the signal phase) are sensitive to the sky signal and the b_m (the quadrature phase) are sensitive to any instrumental effects. The desired number and position of the synthesized lobes on the sky are formed from an appropriate sum of a_m ¹³. Physically, the quadrature

¹³The a_m form a complete set of the sampled spatial frequencies on the sky. The maximum useful m is set by the intrinsic telescope beam size and the spatial sampling rate. The beam synthesis allows the window function sidelobe response to be

phase is the difference between the data taken during the clockwise chopper scan minus the data taken during the counterclockwise scan. We label a synthesized beam by the number of lobes, $n = m + 1$, the receiver waveguide band designation, and observing run year. For example, in SK93K_a, a sinusoidal modulation of the beam was used and a_2 was the only term in the weighting vector. The resulting pattern qualitatively resembles a ‘double-difference’ or ‘three-beam-chop’ and we refer to it as the three-point, or 3pt, response.

As the beam sweeps across the sky, spatial frequencies along the direction of motion are detected over a range of audio frequencies. The anti-aliasing filters and integrators (See Table 4) filter our measurement of the angular power spectrum of the CMB. In 1993, the effect was the largest ($\sim 5\%$) and was corrected in the frequency domain by a direct multiplication of the data. Because the response of the combination of the filters is well approximated by a Gaussian, the effect may also be corrected by allowing σ_{\parallel} (See Equation 16) to be a function of the position in the sweep. In other words, the correction is made as a convolution in the spatial domain. This was done in 1994 and 1995 to correct a 12% effect at the highest frequency.

The data are normalized so a small change in temperature of δT from a 2.7 K blackbody filling the positive lobes of the synthesized beam gives a detected signal of δT . In other words, the synthesized beams are normalized such that the integral of the area under the positive lobes of the effective antenna pattern is equal to one,

$$1 \equiv \frac{1}{2} \int |H(\hat{\mathbf{x}}, n)| \, d\hat{\mathbf{x}}, \quad (14)$$

where H is the oriented antenna pattern for the n -point response. The oriented antenna pattern is

$$H(\hat{\mathbf{x}}, n) \equiv \left\langle \sum_{i=1}^{N_s} w_i(n) G(\hat{\mathbf{x}} - \hat{\mathbf{x}}'(t_i)) \right\rangle, \quad (15)$$

where G is the antenna angular response, $\hat{\mathbf{x}}$ denotes the arrival direction of photons incident on the tele-

tailored, allows optimal filtering of atmospheric and radiometric offset noise, and can facilitate comparison between different observations (e.g. The center of the synthesized beam response can be steered in azimuth from the nominal base position.). In forming a weighting vector with optimal sky sensitivity, the b_n are set equal to zero; by symmetry they do not contribute to a celestial signal.

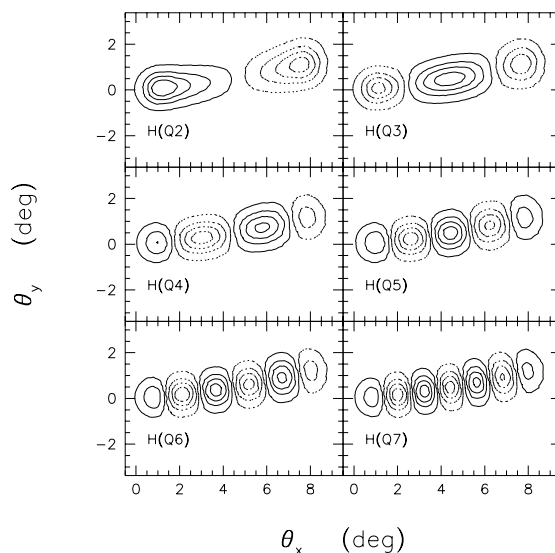


Fig. 7.— Contours of the SK94Q synthesized beam pattern. Dashed and solid lines respectively indicate negative and positive beam lobe responses during a chop cycle. The telescope is in the east base position. Note, lines of constant beam elevation curve upward with respect to lines of constant right ascension. The North Celestial Pole (NCP) is at $(0,0)$, θ_x and θ_y are defined in Table 5.

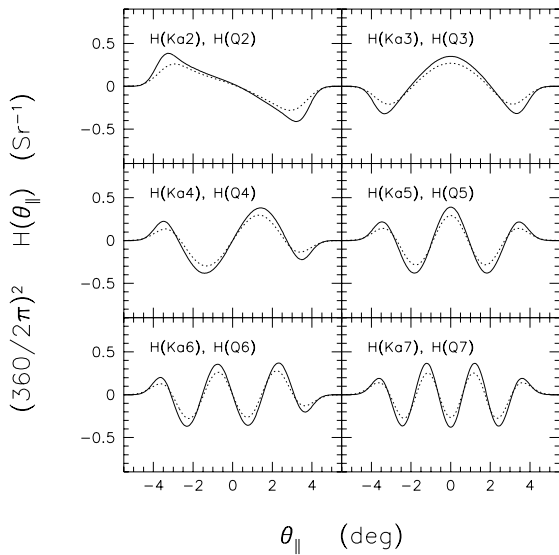


Fig. 8.— Profiles of the SK94 synthesized beam patterns. SK94K_a and SK94Q are indicated by dashed and solid lines respectively. The cut through the synthesized pattern is parallel to the direction of the throw. The origin of θ_{\parallel} is at the chopper center position.

scope, $\hat{\mathbf{x}}'$ is the beam position corresponding to sample t_i as defined in Equation 11, and the brackets indicate an average over the pie-like wedge of an observation¹⁴. We approximate the telescope angular response by a Gaussian,

$$G(\hat{\mathbf{x}}-\hat{\mathbf{x}}') \simeq \frac{1}{2\pi\sigma_{\perp}\sigma_{\parallel}} \exp\left(-\frac{|\mathbf{x}_{\perp}-\hat{\mathbf{x}}'(t_i)|^2}{2\sigma_{\perp}^2}-\frac{|\mathbf{x}_{\parallel}-\hat{\mathbf{x}}'(t_i)|^2}{2\sigma_{\parallel}^2}\right), \quad (16)$$

where $\hat{\mathbf{x}} = \mathbf{x}_{\perp} + \mathbf{x}_{\parallel}$, $\sigma = \theta_{\text{FWHM}}/\sqrt{8\ln(2)}$ is the beamwidth, and ‘ \perp ’ and ‘ \parallel ’ indicate the components perpendicular and parallel to the direction of the chopper throw. The gain is normalized with an effective beam solid angle equal to the best fit to the measured antenna response, $\delta\Omega_{\text{b}} \equiv 2\pi\sigma_{\perp}\sigma_{\parallel}$ (the main beam response has a > 0.98 overlap with a Gaussian spatial distribution). With these conventions, the sig-

¹⁴The n -point data are averaged for either 30 or 60 minutes. As a result, the effective synthesized beam pattern for the final pixel is smeared in right ascension. For atmospheric investigations, the instantaneous oriented antenna pattern is used. The difference between normalizing H with the instantaneous profile and the smeared response is less than 1%.

nal for the j^{th} pixel on the sky is

$$\Delta T_j^{(n)} = \int H(\hat{\mathbf{x}}, n) T_{\text{b}}(\hat{\mathbf{x}}) d\hat{\mathbf{x}}, \quad (17)$$

where T_{b} is the celestial brightness distribution. Typical examples of the resulting beam sensitivities are given in Figures 7 and 8.

The rms of the data depends on the weighting vector used. A measure of this is κ_n , defined as the ratio of the rms of the weighted data to the rms of the raw data,

$$\kappa_n = \left(N_s \sum_{i=1}^{N_s} w_i(n)^2 \right)^{1/2}. \quad (18)$$

Table 8 gives κ_n for all the weighting vectors. The overall sensitivity decreases (κ_n increases) as the synthesized beam spacing approaches the intrinsic telescope beamwidth. In practice, ~ 3 time samples per beam width are required in order to avoid a significant loss of resolution.

The sensitivity of the telescope for a particular weighting scheme is $\kappa_n S_{\nu}(f_{\text{obs}})$, where f_{obs} is the effective sampling frequency associated with the weighting vector (See Table 8) and S_{ν} is the power spectrum of the receiver while staring at the sky (See Figure 3). Although one loses sensitivity for high n , this is partially compensated by the corresponding reduction in instrumental $1/f$ noise with increasing frequency.

5. Radiometric Offsets

We use the following model to identify contributions to the offset:

$$T_{\text{ant}} \simeq (1 - \varepsilon_o) [\eta_{\text{b}} (T_{\text{sky}} + T_{\text{atm}}) + (1 - \eta_{\text{b}}) T_{\text{spill}}] + \varepsilon_o \eta_{\text{b}} T_{\text{plate}}, \quad (19)$$

where $\eta_{\text{b}} \approx 1$ is the beam efficiency, $\varepsilon_o \ll 1$ is the emissivity of the aluminum chopping plate, T_{sky} is the brightness temperature of the sky measured from the surface of the Earth, T_{atm} is the atmospheric brightness temperature, T_{plate} is the physical temperature of the chopping plate, and T_{spill} is the termination temperature of the sidelobes. When the beam is moved on the sky, the change in antenna temperature is

$$\begin{aligned} \delta T_{\text{ant}} \simeq & \delta\eta_{\text{b}} (T_{\text{sky}} + T_{\text{atm}} - T_{\text{spill}}) \\ & + \delta\varepsilon_o \eta_{\text{b}} T_{\text{plate}} + \eta_{\text{b}} (\delta T_{\text{atm}} + \varepsilon_o \delta T_{\text{plate}}) \\ & + (1 - \eta_{\text{b}}) \delta T_{\text{spill}}, \end{aligned} \quad (20)$$

TABLE 8
SK WEIGHTING VECTOR SENSITIVITY, κ_n

n	$\kappa_n(\text{SK93K}_a)$	$\kappa_n(\text{SK94K}_a)$	$\kappa_n(\text{SK94Q})$	$\kappa_n(\text{SK95Q})$
2	2.337	2.280	2.250	2.238
3	3.081	2.512	2.355	2.327
4	.	3.010	2.573	2.451
5	.	3.812	2.938	2.441
6	.	5.026	3.433	2.555
7		6.890	4.079	2.738
8		9.845	4.944	2.813
9		14.67	6.115	3.007
10		.	.	3.121
11		.	.	3.370
12		.	.	3.550
13				3.859
14				4.121
15				4.535
16				4.867
17				5.405
18				5.836
19				6.619

NOTE.—The frequency corresponding to the dominate spectral component of w_i is given by $f_{\text{obs}} \simeq (n - 1) f_c$ where the chopper frequency is $f_c \simeq 3.906$ Hz for SK93K_a and SK94K_a/Q and 2.970 Hz for SK95Q.

where contributions are grouped by changes in coupling efficiency, emission, and termination temperature¹⁵. For simplicity, the sky is assumed to be uniform and only the dominant contributions to the offset are retained. Offsets due to modulated spill-over radiation are controlled by baffle geometry and illumination level. Under-illuminated of the optical elements results in $\delta\eta_b \approx 0$. The offsets from atmospheric emission are minimized through telescope alignment and by rapidly differencing regions with the same temperature. Under stable atmospheric conditions, the dominant contributions are due to modulation of the antenna spill and plate emissivity.

5.1. The Chopping Plate Emission Offset

The process of scanning with the chopper produces a synchronous modulation of the plate emissivity when viewed from the feed. As the angle of incidence is varied, the magnitude of the chopper's surface brightness temperature changes. For good conductor with skin depth $\delta = (1/\mu_o\pi\nu_o\sigma)^{1/2}$, where σ is the conductivity of the metal surface and ν_o is the observing frequency, the parallel and perpendicular emissivities are

$$\varepsilon_{\parallel} \simeq \varepsilon_o / \cos(\theta_i), \quad (21)$$

with $\delta/\lambda_o \ll \cos(\theta_i)$, and

$$\varepsilon_{\perp} \simeq \varepsilon_o \cos(\theta_i), \quad (22)$$

with $\delta/\lambda_o \ll 1$. The incident angle of the radiation is given by

$$\theta_i(\phi_c) = \cos^{-1} \left(-\hat{\mathbf{k}}_i \cdot \hat{\mathbf{n}}(\phi_c) \right), \quad (23)$$

where $\hat{\mathbf{k}}_i$ is the propagation vector and $\hat{\mathbf{n}}$ is the plate normal vector in the detector frame. (e.g. Landau & Lifshitz 1960; Rytov, Kravtsov, & Tatarskii 1978). The emissivity of a 6061-T6 aluminum sheet at 31.4 GHz is $\varepsilon_o \equiv 4\pi\delta/\lambda_o \approx 9 \times 10^{-4}$. We normalized Equations 21 and 22 to the DC conductivity of the surface¹⁶. The brightness temperature of the

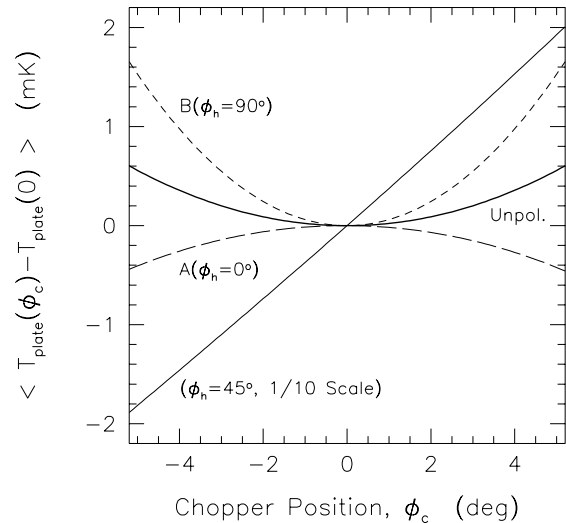


Fig. 9.— The antenna temperature due to plate emission as a function of chopper azimuthal position. In the field, feed polarization ‘A’ (long dashes) is vertical and ‘B’ (short dashes) is horizontal. For this calculation, the observation angle is $\theta_z = 37.85^\circ$ and the radial extent of the plate is taken as infinite. A physical temperature of $T_{\text{phys}} = 300$ K and an emissivity of $\varepsilon_o = 9 \times 10^{-4}$ are assumed. The solid line is 1/10 of the computed magnitude for the feed polarization with $\phi_h = 45^\circ$. The response of an ideal unpolarized detector is indicated by the solid bold line. The average emission for a fixed incidence angle, $260 < \langle T_{\text{plate}} \rangle < 430$ mK, is a function of the feed polarization orientation. To facilitate comparison, this constant term has been subtracted from the computed response. Calculated and measured magnitudes are given in Table 9.

¹⁵Modulation of the receiver input match can also produce synchronous offsets. The beam switch in the SK telescope is produced by both the chopper and the base motions. Due to the off-axis telescope geometry and relatively wide channel bandwidth, the receiver noise temperature and amplitude response are essentially unmodulated by switching.

¹⁶Due to the differences in the DC conductivity of aluminum, the relative emissivity varies by a factor upto ~ 1.5 depending upon alloy type (e.g. Weast 1982). Surface treatment and finish can increase the RF emissivity by an additional factor between 1.1 and 1.5 in typical microwave components.

TABLE 9
MEASURED AND ESTIMATED AVERAGE RADIOMETRIC OFFSETS

Component	SK93K _a A/B [μ K]	SK94K _a A/B [μ K]	SK94Q A/B [μ K]	SK95Q A/B [μ K]
ΔT_{plate}	+50/ - 190	+120/ - 430	+130/ - 500	+150/ - 570
ΔT_{atm}	-150	-5	-10	-10
ΔT_{spill}	-10	-10	-10	\sim -500
ΔT_{theory}	-110/ - 350	+105/ - 445	+110/ - 520	...
$\Delta T_{\text{observed}}$	-60/ - 360	+117/ - 550	... / - 695	-616/ - 2182

NOTE.—The three-point offsets are computed from the measured plate emissivity, telescope alignment, and spill. ΔT_{spill} is an order of magnitude estimate based on the telescope configuration. The theoretical offset is estimated from $\Delta T_{\text{theory}} = \Delta T_{\text{plate}} + \Delta T_{\text{atm}} + \Delta T_{\text{spill}}$ using the measured telescope parameters. The offset for the SK95Q three-point is larger than the simple model used here would predict. We believe the excess offset is due to a 0.04 cm wide seam in one side of the chopper which moves laterally with respect to the center of the beam during a chop cycle.

plate is

$$T_{\text{plate}} \simeq T_{\text{phy}} \left[\varepsilon_{\parallel}(\theta_i) \left| \tilde{\mathbf{E}}_{\parallel}(\theta_i) \right|^2 + \varepsilon_{\perp}(\theta_i) \left| \tilde{\mathbf{E}}_{\perp}(\theta_i) \right|^2 \right], \quad (24)$$

where T_{phy} is the physical temperature of the plate, and $\tilde{\mathbf{E}}_{\parallel}$ and $\tilde{\mathbf{E}}_{\perp}$ are the perpendicular and parallel electric field projections onto the chopping flat normal. The resulting emission can be expressed as

$$\Delta T_{\text{plate}}^{(n)} \simeq \int H(\hat{\mathbf{x}}, n) T_{\text{plate}}(\hat{\mathbf{x}}) d\hat{\mathbf{x}}, \quad (25)$$

where H is the antenna pattern of the synthesized beam (See Section 4). Since the chopping plate essentially fills the entire field of view, the emission offset is only a function the chopper position angle and the weighting vector. The antenna temperature as a function of the physical chopper position angle with $w_i = 1$, is given in Figure 9. For polarization $\phi_h = 0^\circ$ (E vector \perp to the chopper axis) and 90° , the anti-symmetric component of the offset is eliminated. With $\phi_h = \pm 45^\circ$ the symmetric term is minimized. For an unpolarized detector, the anti-symmetric component is eliminated by the average over feed polarization angle. The measured and computed three-point offset for each radiometer is summarized in Table 9.

With $\phi_h = \pm 45^\circ$, the two-point offset was measured to be $\delta \Delta T_{\text{plate}} / \delta \phi_c \approx \pm(3.3 \pm 0.3) \text{ mK deg}^{-1}$. The predicted magnitude is $\sim 3.5 \text{ mK deg}^{-1}$ for the aluminum chopping plate surface. In the vertical & horizontal feed polarization configuration ($\phi_h = 0^\circ$ and 90°) a stainless steel sheet was rigidly attached to the chopper surface. The measured offset increased by a factor of ~ 7 consistent with the increase in emissivity.

Changes in the plate temperature influence the offset magnitude. The chopping flat temperature is monitored at 7 locations. While taking astrophysical data, the average chopping plate temperature varied by as much as 30 K. This results in a maximal $\pm \sim 5\%$ variation in the offset magnitude as a function of the ambient temperature. There is a small correlation between the chopper temperature and the offset. However, changes in ambient temperature can effect the offset through other mechanisms (See Section 5.4) so one cannot conclude that the correlation is causal. Removal of the correlated signal has negligible effect on the reported results.

5.2. The Chopping Plate Spill Offset

As the plate moves, the chopper edge diffraction changes. This effect is minimized by under-illuminating the flat. By evaluating the directivity in the Gaussian optics approximation we obtain an estimate of the chopper edge illumination (Martin 1990; also see, Murphy, Egan, & Withington 1993); for the SK93 optics it is -46 dB relative to the near field main beam, consistent with measurement. In addition, a stationary baffle that extends 15 cm past the chopper edge shields the chopper from behind. The computed illumination level at this edge is more than -65 dB lower than the main beam in the chopper plane. For the SK93 and SK94 optical designs, the offset due to modulated spill is immeasurably small. For SK95, the edge illumination was increased to produce a narrower beam. This contributed to the larger 3pt offset that year.

5.3. The Atmospheric Offset

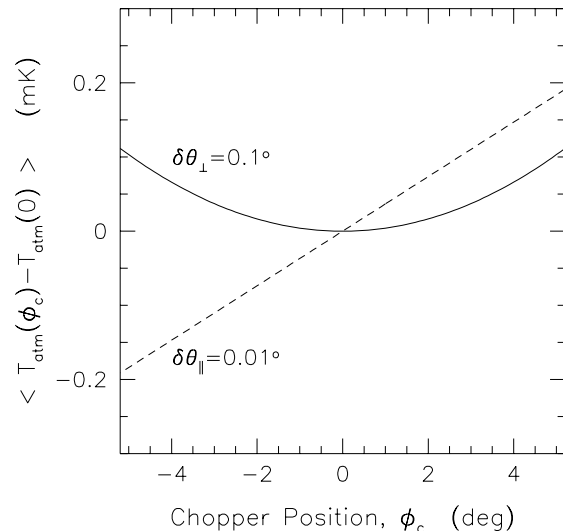


Fig. 10.— The atmospheric antenna temperature due to misalignment of the chopper rotational axis as a function of chopper azimuthal position. A zenith temperature of $T_z = 10 \text{ K}$ is assumed. Typical axis misalignment errors, $\delta\theta_{\perp} = 0.1^\circ$ and $\delta\theta_{\parallel} = 0.01^\circ$ are indicated by solid and dashed lines respectively. The three-point offset (inner minus outer lobes), is negative for a positive elevation error.

The chopping plate axis is aligned with the vertical

in order to minimize the atmospheric offset, ΔT_{sky} . If the plate axis is rotated in the plane of the plate, $\delta\theta_{\parallel}$, a two-point response will be generated. A base or chopper throw leveling error would induce this offset. A vertical axis error due to a rotation perpendicular to the plane of the plate, $\delta\theta_{\perp}$, generates a three-point response. A typical example of this is an elevation pointing error. We model atmospheric brightness temperature as

$$T_{\text{atm}} = \langle T_{\text{atm}} \rangle + \frac{\partial T_{\text{atm}}}{\partial \psi} [\delta\psi_{\parallel} + \delta\psi_{\perp}], \quad (26)$$

where $\delta\psi \ll 1$ is the variation in angle due to chopper misalignment from a fixed zenith angle. We assume a gradient in the atmospheric temperature of the form

$$\frac{\partial T_{\text{atm}}}{\partial \psi} \simeq T_z \tan(\theta_z) \sec(\theta_z), \quad (27)$$

where T_z is the zenith temperature. The variation in the sky signal due to a small rotation about the axis parallel to the chopper normal is approximated by

$$\delta\psi_{\parallel} \simeq 2\delta\theta_{\parallel} \sin(\theta_z) \sin(\phi_c), \quad (28)$$

where $\delta\theta_{\parallel} \ll 1$. The leading factor of 2 results from the reflection of the beam off the plate. Similarly, for a small rotation of the chopper vertical axis about the perpendicular to the plate normal

$$\delta\psi_{\perp} \simeq -2\delta\theta_{\perp} \cos(\theta_z) \cos(\phi_c), \quad (29)$$

for $\delta\theta_{\perp} \ll 1$. From Equation 26, the resulting atmospheric offset is

$$\Delta T_{\text{atm}}^{(n)} \simeq \int H(\hat{\mathbf{x}}, n) T_{\text{atm}}(\hat{\mathbf{x}}) d\hat{\mathbf{x}}. \quad (30)$$

In Figure 10, the atmospheric brightness temperature as a function of chopper position is plotted for typical chopper alignment errors. In practice, temporal variations in the horizontal atmospheric temperature profile can mask the effects of the parallel axis misalignment on short time scales.

5.4. Limits to Offset Stability

The stability of the offset is as important as its magnitude. For example, *COBE/DMR* had offsets on the order of hundreds of milli-Kelvin (Kogut et al. 1992) but the extreme stability of the space environment allowed it to produce the highest quality data set to date. Stability is especially important for the

SK experiment because the sky is re-observed only every 12 hours. Possible causes for a drift include changes in the chopping plate temperature profile, thermal contraction of the mounts, icing of the optics, and changes in the system gain from thermal variations. The largest drift is $7 \mu\text{K}/\text{day}$ in the SK95 three-point data, more typically the drift is $< 4 \mu\text{K}/\text{day}$.

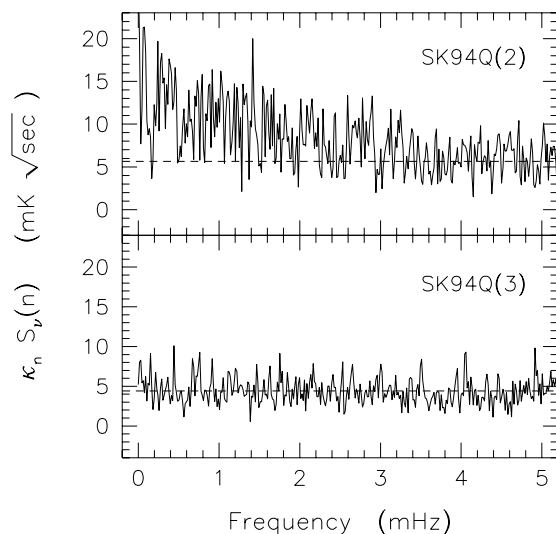


Fig. 11.— The power spectrum of the weighted data (SK94Q: $\zeta < 2.5 \text{ mK sec}^{\frac{1}{2}} \text{ deg}^{-1}$). The dashed lines indicate the detector sensitivity. The 2pt data, taken at 4 Hz and labeled SK94Q(2), have a substantial atmospheric contribution, while the 3pt (and higher) data are detector noise limited. The offset for the channel was subtracted before taking the Fourier transform.

There may be drifts in the data on faster time scales but the receivers are not sensitive enough to detect them. In 12 hours, the 3pt SK94Q data (Figure 11) can only measure $20 \mu\text{K}$ with a signal-to-noise of one. Even when data from multiple channels are combined, the noise is not reduced by more than two. If there are short time scale drifts, then they must average out because we observe the same signal on the sky in subsections of the data and in multiple years. The problem of offset removal is addressed in Netterfield et al. 1996.

6. Atmospheric Noise and Data Editing

During January through March, Saskatoon is relatively dry, clear, and cold. Precipitable water vapor has a mean value of 5 mm and drops to ≤ 2 mm on the coldest winter days (Jones 1993). From ground-based measurements of the wind speed/direction, temperature, pressure and relative humidity at the site, the following general trends were noted: ‘good data’ are typically obtained during periods with little or no wind (< 5 knots), temperatures less than -5°C , atmospheric pressure greater than 710 Torr, stable weather systems, and low relative humidity. However, at times the effects of atmospheric turbulence were seen in the data despite clear skies and favorable weather station readings, suggesting that the offending fluctuations were far removed from the telescope. In general, the presence of high altitude clouds or ice fog did not increase the atmospheric noise.

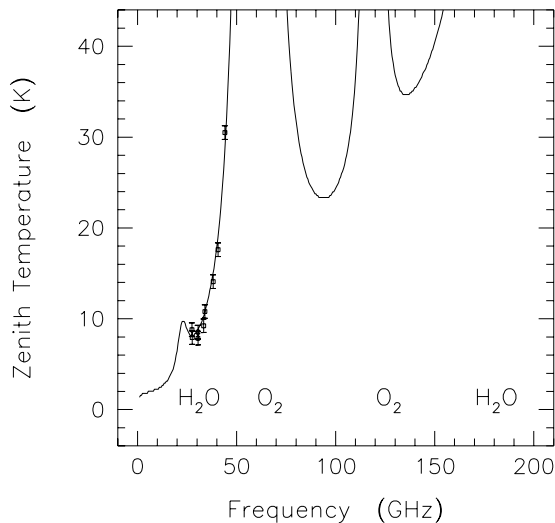


Fig. 12.— The atmospheric zenith temperature in Saskatoon, SK on a typical calm winter day. The units are antenna temperature and the error bars reflect the uncertainty in the calibration scale. The solid curve is the modeled radiometric brightness temperature.

The atmospheric zenith temperature is measured by tilting the chopping plate $\pm 5^\circ$ and measuring the total power at the detector. Using the Van Vleck-Weisskopf line shape, we compute the theoretical atmospheric zenith temperature assuming a $\sec(\theta_z)$ de-

pendence for the column depth (Liebe 1985; Danese & Partridge 1989). The results are presented in Figure 12. Data suitable for CMB analysis lay within a ~ 4 K atmospheric temperature window above the minimum recorded magnitude at the site.

In addition to the flat spectral component from atmospheric thermal emission, there is also a ‘ $1/f$ ’ component originating from atmospheric turbulence (Tatarski 1961, Andreani et al. 1990, Church 1995). There also appear to be other mechanisms that enter on longer time scales. The spatial power spectrum of the emission is dominated by thermal gradients spanning $> 4^\circ$ as determined from the 2pt data. These gradients have been observed to persist for up to an hour. The 3pt data, which are sensitive to the curvature rather than the gradient, are typically have a factor of eight less noise.

The atmospheric cut for selecting astrophysical data (3pt and higher) is based on the stability of the statistically independent 2pt data. This is done by evaluating the 2pt mean deviation, η , of the 8 second averages for a 20 minute segment of data. The mean deviation is less sensitive than the standard deviation to outliers. To compare with other experiments, the cut levels are converted to units of $\text{mK sec}^{\frac{1}{2}} \text{deg}^{-1}$ by multiplying η , by the sensitivity of the synthesized beam pattern to a 1 mK deg^{-1} horizontal atmospheric gradient,

$$\zeta \equiv \frac{\kappa_2}{\theta_{\text{eff}}} \text{NET}_{\text{atm}} \approx \sqrt{\frac{\pi}{2}} \frac{\eta \sqrt{\tau}}{\theta_{\text{eff}}}, \quad (31)$$

where NET_{atm} is the equivalent noise temperature of the cut level, τ is the integration time, and $\theta_{\text{eff}} = \int \theta_{\parallel}(\hat{\mathbf{x}}) H(\hat{\mathbf{x}}, 2) d\hat{\mathbf{x}}$ is the 2pt effective beam separation angle. This conversion assumes Gaussian fluctuations which is not necessarily valid. Figure 13 shows the distribution of the spatial gradient fluctuations, ζ , at several cut levels.

The distributions from K_a and Q have some qualitative differences. The lower cut off on both distributions is due to the system noise, which is higher in Q than K_a . The second hump located in the vicinity of $\sim 200 \text{ mK sec}^{\frac{1}{2}} \text{deg}^{-1}$ is due to data acquired during a two week period of very poor weather in January 1994. Similarly, the bump in SK93 results from data taken during the spring thaw in March of 1993. During these periods the zenith temperature is unstable and the atmospheric water content relatively high.

For roughly 25% of any campaign, the receivers are detector noise dominated (Netterfield et al. 1996).

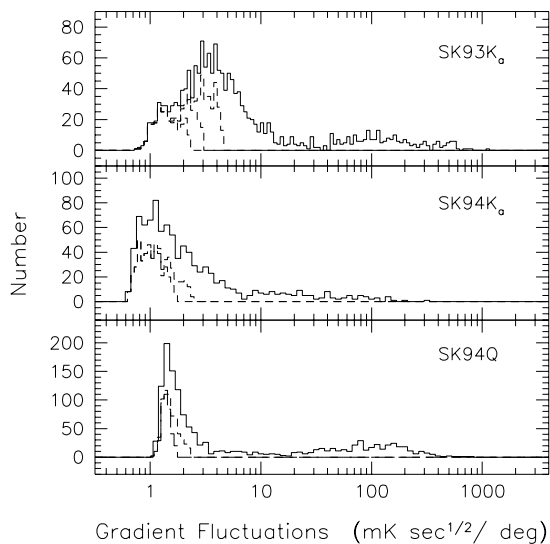


Fig. 13.— The distribution of fluctuations for 20 minute averages of the two-point data as a function of cut level: SK93K_a with the 27.5 GHz channel, $\zeta = 2.2, 3.0, 4.5$, and all data; SK94K_a, $\zeta = 1.7, 2.5$, and all data; and SK94Q with the 38.5 GHz channel, $\zeta = 1.7, 2.5$, and all data. Horizontal units are $\text{mK sec}^{\frac{1}{2}} \text{deg}^{-1}$ (antenna temperature). The receiver noise floors for 1993 and 1994 K_a were the same; however, with the increased chopper throw in 1994, the sensitivity to atmospheric fluctuations increased. To convert to the equivalent $\text{NET}_{\text{atmos}}$ multiply by, $\theta_{\text{eff}}/\kappa_2 = 1.68^\circ$, for SK93K_a, $\theta_{\text{eff}}/\kappa_2 = 2.25^\circ$, for SK94K_a, and for SK94Q, $\theta_{\text{eff}}/\kappa_2 = 2.37^\circ$. Note that the receiver noise contribution is included in ζ .

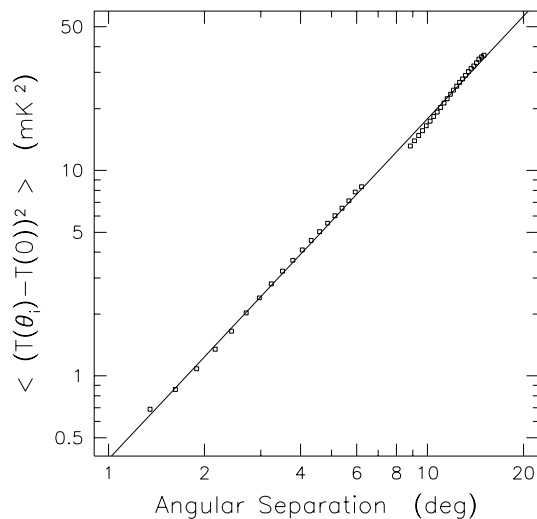


Fig. 14.— The atmospheric noise structure function. The boxes are a 20 min average of the structure function (SK94Q: $\zeta < 2.5 \text{ mK sec}^{\frac{1}{2}} \text{deg}^{-1}$). The solid line ($\log\langle(T(\theta_i) - T(0))^2\rangle = 1.66 \log(\theta_i) - 0.41$) is a fit to the data.

As an example of the atmospheric stability, the power spectrum for an 18 Hr contiguous stretch of good data ($\zeta < 2.5 \text{ mK sec}^{\frac{1}{2}} \text{deg}^{-1}$) is shown in Figure 11. The two-point response, SK94Q(2), has a $1/f$ knee of $\sim 1 \text{ mHz}$ and the three-point, SK94Q(3), is featureless. For $n > 2$ the responses are qualitatively similar to SK94Q(3). In Figure 14, the structure function, $D(\theta_i) \equiv \langle(T(\theta_i) - T(0))^2\rangle$ (See Tatarski 1961, Church 1995), is computed for a 20 minute average of the data. For beam separations less than 7° , the average of the east and west data sets is used, while for angles greater than 7° , the east and west data are combined into a long scan across the sky. The absence of evidence of saturation in $D(\theta_i)$ suggests this component of the atmospheric noise results from angular scales greater than the base wobble angle.

7. Summary

The instrument uses a HEMT-based total-power receiver at the focus of an off-axis parabolic primary. The beam is swept many beamwidths on the sky with a large under-illuminated movable flat. The clear optical path, polarization orientation, and mechanical stability result in small and stable radiometric offsets.

To provide spectral discrimination, each receiver observes in three frequency bands. The radiometer outputs are sampled rapidly compared to the beam scan rate. This is possible because of the fast response of the detectors. By weighting each sample in software, a set of synthesized beams is constructed. This allows one to simultaneously probe a range of angular scales, optimize spatial frequency coverage while minimizing atmospheric contamination, and synthesize beam patterns for a direct comparison with other experiments.

The data from this instrument are of generally high quality and we are not aware of any instrument-based systematic effects that could compromise them. The data selection criteria are not based on the data used for the astrophysical analysis but rather on an independent weighting scheme. Also, the symmetries in the observing strategy and the three years of observations provide many internal consistency checks. The dominant contribution to the 14% calibration uncertainty is from the inaccuracy in our knowledge of our calibration source, Cas-A. Future observations using the techniques described here will enhance our confidence in the data and lead to a better understanding of the anisotropy in the CMB.

8. Acknowledgments

We gratefully acknowledge the contribution and support of many people associated with this project. We are indebted to Marian Pospieszalski and Mike Balister of NRAO for providing the HEMT amplifiers. George Sofko, Mike McKibben at the University of Saskatchewan's Institute for Space and Atmospheric Studies, and Larry Snodgrass at the Canadian SRC provided valuable assistance in the field. We also thank Chris Barnes, Carrie Brown, Weihseh Chiu, Randi Cohen, Peter Csatorday, Cathy Cukras, Peter Kalmus, John Kulvicki, Wendy Lane, Young Lee, Glen Monnelly, Rob Simcoe, Jenő Sokoloski, Naser Quershi, Peter Wolanin and the Princeton University shop for their help in constructing the apparatus. Discussions with Sarah Church, Brian Crone, Dale Fixsen, Tom Herbig, John Ruhl, and Suzanne Staggs are greatly appreciated.

This research was supported by NSF grant PH89-21378, NASA grants NAGW-2801 and NAGW-1482, and a Packard Fellowship, a Research Corporation Award, and an NSF NYI grant to L. Page.

REFERENCES

- Allen, C. W. 1976, *Astrophysical Quantities*, (London: Athlone Press), 3rd edition
- Andreani, P., Dall'Oglio, G., Martinis, L., Piccirillo, L., Pizzo, L., & Rossi, L. 1990, *Infrared Phys.*, 30(6), 479
- Baars, J. W. M., Genzel, R., Pauliny-Toth, I. I. K., & Witzel, A. 1977, *Astron. Astrophys.*, 61, 99
- Becker, R. H., White, R. L., & Edwards, A. L. 1991, *ApJS*, 75, 1
- Bond, J. R. 1995. Theory and observations of the cosmic background radiation in *Cosmology and Large Scale Structure: Proc. Les Houches School Session LX, Aug. 1993*, ed. R. Schaeffer. Elsevier Science Publishers, Netherlands
- Bond, J. R., Crittenden, R. R., Davis, R. L., Efstathiou, G., & Steinhardt, P. J. 1994, *Phys. Rev. Lett.*, 72(1), 13
- Church, S. E. 1995, *MNRAS*, 272, 551
- Clarricoats, P. J. B. & Olver, A. D. 1984, *Corrugated Horns for Microwave Antennas*, (London: Peter Peregrinus Ltd.)
- Crone, B. 1993. Princeton University Physics, Princeton, NJ. Private Communication
- CTI. Operator's Manual CryodyneTM Helium Refrigerator, Model 350. Cryogenic Technology, Waltham, MA 1971
- Dall'Oglio, G. & de Bernardis, P. 1988, *ApJ*, 331, 547
- Danese, L. & Partridge, R. B. 1989, *ApJ*, 342, 604
- Davies, R. D., Lasenby, A. N., Watson, R. A., Daintree, E. J., Hopkins, J. and Beckman, J., Sanchez-Almeida, J., & Rebolo, R. 1987, *Nature*, 326, 462
- Dicke, R. H. 1946, *Rev. Sci. Instrum.*, 17, 268
- Dodson, S., Kosowsky, A., & Myers, S. T. 1994, *ApJ*, 440, L37
- Dragone, C. 1977, *Bell Sys. Tech. J.*, 56(6), 869
- Dragone, C. & Hogg, D. C. 1963, *Bell Sys. Tech. J.*, 42(5), 1

- Dragovan, M., Ruhl, J. E., Novak, G., Platt, S. R., Crone, B., Pernic, R., & Peterson, J. B. 1994, *ApJ*, 427, L67
- Fabbri, R., Guidi, I., Melchiorri, F., & Natale, V. 1980, *Phys. Rev. Lett.*, 44(23), 1563
- Fich, M. 1986, *ApJ*, 92, 787
- Fixsen, D. 1995. Goddard Space Flight Center, Greenbelt, MD. Private Communication
- Friberg, A. T., Jaakkola, T., & Tuovinen, J. 1992, *IEEE Trans. Antennas Propagat.*, AP-40(8), 984
- Gaier, T., Schuster, J., Gundersen, J., Koch, T., Seifert, M., Meinhold, P. R., & Lubin, P. M. 1992, *ApJ*, 398, L1
- Gundersen, J. et al. 1994. A preliminary analysis of UCSB's South Pole 1993-94 results in CMB Anisotropies Two Years After COBE: Observation, Theory, and the Future, ed. L. M. Krauss. World Scientific, Singapore
- Gush, H. et al. 1990, *Phys. Rev. Lett.*, 65(5), 537
- James, G. L. & Thomas, B. M. A. 1982, *IEEE Trans. Microwave Theory and Tech.*, MTT-30(3), 278
- Jarosik, N., Page, L., Wilkinson, D., & Wollack, E. 1993. Measurements of the low frequency noise properties of a 30 Ghz high-electron-mobility-transistor amplifier. Technical Report 95955, Princeton University
- Jones, K. 1993. Meteorological summary. Technical report, Environment Canada, Saskatoon, SK
- Jungman, G., Kamionkowski, M., Kosowsky, A., & Spergel, D. submitted to PRL 1995, Harvard-Smithsonian Center for Astrophysics, preprint 4136
- Kallas, E. & Reich, W. 1980, *Astron. Astrophys. Suppl. Ser.*, 42, 227
- Keller, J. B. 1959, *J. Appl. Phys.*, 30, 1452
- Kogut, A. et al. 1992, *ApJ*, 401, 1
- Kuo, B. J. 1991, *Automatic Control Systems*, 6th Ed., (Englewood Cliffs, NJ: Prentice Hall)
- Landau, L. D. & Lifshitz, E. M. 1960, *Electrodynamics of Continuous Media*, (Oxford: Pergamon Press)
- Liebe, H. J. 1985, *Radio. Sci.*, 20(5), 1069
- Lubin, P. M., Epstein, G. L., & Smoot, G. F. 1983, *Phys. Rev. Lett.*, 50(8), 616
- Martin, D. H. 1990. Quasi-optics: Modal analysis of free-space propagation in Recent Advances in Antenna Theory and Design, MEPL Reprint Series, ed. P. Clarricoats & C. Parini. Microwave Exhibitions and Publishers Ltd.
- Mather, J. C. et al. 1994, *ApJ*, 420, 439
- Matthaei, G., Young, L., & Jones, E. 1980, *Microwave Filters, Impedance Matching Networks and Coupling Structures*, (Boston: Artech House)
- Mezger, P. G., Tuffs, R. J., Chini, R., Kreyza, E., & Gemünd, H. P. 1986, *Astron. Astrophys.*, 167, 145
- Murphy, J. A., Egan, A., & Withington, S. 1993, *IEEE Trans. Antennas Propagat.*, AP-41(10), 1408
- Myers, S. T., Readhead, A. C. S., & Lawrence, C. R. 1993, *ApJ*, 405, 8
- Netterfield, C. B. 1995. PhD thesis, Princeton University
- Netterfield, C. B., Devlin, M. J., Jarosik, N., Page, L., & Wollack, E. J. 1996, *ApJ*, submitted
- Netterfield, C. B., Jarosik, N., Page, L., Wilkinson, D., & Wollack, E. 1995, *ApJ*, 445, L69
- Page, L. A. et al. 1994. Observations of the anisotropy in the cosmic microwave background by the FIRS, SK93, and MSAM-I experiments in CMB Anisotropies Two Years After COBE: Observation, Theory, and the Future, ed. L. M. Krauss. World Scientific, Singapore
- Partridge, B. & Wilkinson, D. T. 1967, *Phys. Rev. Lett.*, 18, 557
- Payne, J. 1976, *Rev. Sci. Instrum.*, 47(2), 222
- Pospieszalski, M. W. 1992, *Proc. IEEE MTT-S Int. Microwave Symp.*, 3, 1369
- Pospieszalski, M. W., Weinreb, S., Norrod, R. D., & Harris, R. 1988, *IEEE Trans. Microwave Theory and Tech.*, MTT-36(3), 552
- Pozar, D. M. 1990, *Microwave Engineering*, (New York: Addison-Wesley)

- Radford, S. J. . E., Boynton, P., & Melchiorri, F. 1990, *Rev. Sci. Instrum.*, 61, 3
- RCB 1993. Quarterly publication of the space network list. Technical Report 30.03.93, International Telecommunication Union
- Readhead, A. C. S. & Lawrence, C. R. 1992, *ARA&A*, 30, 653
- Rohlfs, K. 1990, *Tools of Radio Astronomy*, (Berlin: Springer-Verlag)
- Rudge, A. W. & Adatia, N. A. 1978, *Proc. IEEE*, 66(12), 1592
- Rudge, A. W., Milne, K., Olver, A. D. & Knight, P. 1982. *The Handbook of Antenna Design*, volume 1, chapter 3. Peter Peregrinus Ltd.
- Ruze, J. 1966, *Proc. IEEE*, 54(4), 633. AFCRC TR 57-105; *Antenna Tolerance Theory—A Review*
- Rytov, S. M., Kravtsov, Y. A., & Tatarskii, V. I. 1978, *Principles of Statistical Radiophysics 3: Elements of Random Fields*, (Moscow: Nauka)
- Silver, S. 1949, *Microwave Antenna Theory and Design*, (New York: Mc Graw–Hill)
- Sletten, C. J., p. 1988, *Reflector and Lens Antennas*, (Boston: Artech House)
- Tatarski, V. 1961, *Wave Propagation in a Turbulent Medium*, (New York: Mc Graw–Hill)
- Thomas, B. M. 1978, *IEEE Trans. Antennas Propagat.*, AP-26(2), 367
- Timbie, P. T. & Wilkinson, D. T. 1990, *ApJ*, 353, 140
- Tuovinen, J. 1992, *IEEE Trans. Antennas Propagat.*, AP-40(4), 391
- Weast, R. C. 1982, *Handbook of Chemistry and Physics*, (Boca Raton, FL: CRC Press), 63 edition
- White, M., Scott, D., & Silk, J. 1994, *ARA&A*, 32, 319
- Wollack, E. J. 1994. PhD thesis, Princeton University
- Wollack, E. J. 1995, *Rev. Sci. Instrum.*, 66(8)
- Wollack, E. J., Jarosik, N., Netterfield, B., Page, L., & Wilkinson, D. 1994, *Astrophys. Lett. Commun.*, 35, 217
- Wollack, E. J., Jarosik, N. C., Netterfield, C. B., Page, L. A., & Wilkinson, D. 1993, *ApJ*, 419, L49